HOCHSCHULE KOBLENZ
UNIVERSITY OF APPLIED SCIENCES

DLR Deutsches Zentrum für Luft- und Raumfahrt
German Aerospace Center

Investigation of a Plastic Printed Slotted Waveguide Antenna for Airborne SAR Applications

Bachelor Thesis

by

Jan Reifenhäuser
Student ID: 531145

March 28, 2019

Koblenz University of Applied Sciences
Information Technology
Examiner: Prof. Dr. Uwe Gärtner

German Aerospace Center
Microwaves and Radar Institute
Supervisor: Dipl.-Ing. Markus Limbach

ABSTRACT

With the Ka-band PolInSAR system, the German Aerospace Center is taking a first step towards SAR technology in Ka-band. Thereby, high demands on the mechanical accuracy of complex antenna components require new manufacturing methods such as 3D printing.

Due to a higher coefficient of thermal expansion, an increased sensitivity of the plastic printed antenna against temperature changes is expected. The aim of this work is to investigate the behavior of two antenna prototypes manufactured of brass and plastic in the temperature range of airborne SAR systems.

The investigation is carried out by simulations as well as by practical measurements. The theoretical investigation is performed to analyze the impact of temperature variation on the electrical performance of the prototypes. After the development of a suitable measuring setup, the characteristic of the antennas is measured at different temperatures.

The comparison of a plastic printed and a classical milled antenna showed only minor differences in the electrical behavior and confirms that plastic is suitable for slotted waveguide antennas. Furthermore, a method to detect changes in antenna characteristics within a wide temperature range using simple measuring and processing methods could be introduced.

Keywords: plastic printed antenna, slotted waveguide, influence of temperature, thermal expansion, antenna measurement, time gating

TABLE OF CONTENTS

LIST OF FIGURES

LIST OF TABLES

CHAPTER 1

INTRODUCTION

This chapter gives an overview of the project and introduces to the problem statement of this thesis. It briefly introduces the German Aerospace Center (DLR) and its Synthetic Aperture Radar (SAR) missions. Thereafter, DLR's new objectives in the airborne SAR area are presented and associated problems are discussed.

1.1 SAR Missions of the German Aerospace Center

1.1.1 The German Aerospace Center

The German Aerospace Center is a research facility in the Federal Republic of Germany. It consists of a variety of institutes on 20 different locations in Germany, with a research focus on aeronautics, space, energy, transport, digitization, security and space administration.

The Microwaves and Radar Institute is dedicated to the research of new technologies in the field of radar sensors for remote sensing purposes. Its research focus is on airborne and satellite based radar systems with synthetic aperture.

1.1.2 Synthetic Aperture Radar

A radio detection and ranging (RADAR) system transmits an electromagnetic wave and detects the backscattered wave on objects. The properties of the reflected wave such as amplitude, phase, polarization or Doppler shift can be used to draw conclusions about the reflecting object. Parameters, that can be obtained by this method, range from direction and distance to the object up to its velocity, size and surface condition. Radar systems can be operated in different modes and frequency ranges.

A popular application of radar systems is a remote sensing of the earth's surface. Such systems provide a variety of data that can be converted into digital maps

and provide, among others, information about altitude, topographic changes, forest heights, biomass or soil moisture, whereby the required image resolution is often less than one meter. In general, the angular resolution of a radar system depends on the size of its aperture. Real aperture radar systems, however, cannot fulfill the image resolution required for earth observation, which has been visualized in a descriptive example by Curlander and McDonough: If one imagines a satellite with an antenna size of 10 m at an altitude of 800 km, its resolution cell on earth's surface at a wavelength of 24 cm is about 20 km. In order to achieve a resolution of 25 m, the antenna would have to be extended to a length of 8 km. Whereas these dimensions cannot be realized as a discrete antenna, it can be achieved by moving the radar sensor alongside the object and synthesizing individual samples into an overall image. This method is called synthetic aperture radar (SAR). The radar system is often placed on a satellite or airplane, with the radar beam directed oblique to earth's surface while moving along the flight path [2].

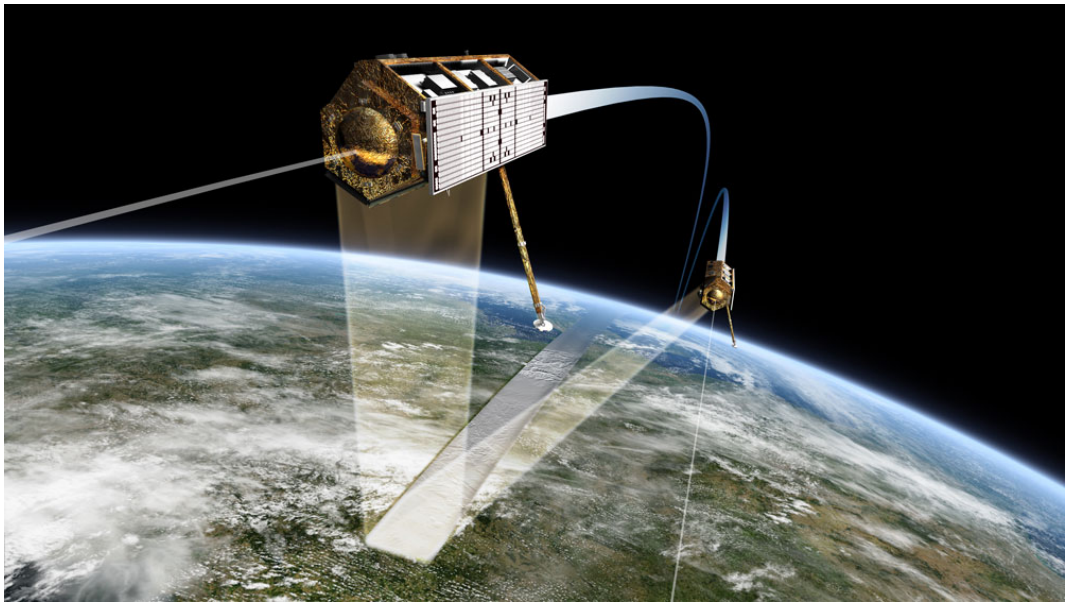

Figure 1.1: TanDEM-X and TerraSAR-X SAR satellites, flying in formation to create an interferometric system.

An extension of this system is SAR interferometry where the same scene is imaged by two radar sensors flying in a distance to each other. By the principle of interferometry the altitude of objects can be determined very precisely which is particularly useful for creation of digital elevation models.

The radar signal can be radiated in alternation with horizontal or vertical polarization in order to obtain more precise information about the surface condition.

When reflected on ground, the polarization may change depending on the reflecting surface. This change is detected upon receiving the echo and conclusions can be drawn about the surface. This procedure is called polarimetry.

1.1.3 DLR's Airborne SAR System

The Microwaves and Radar Institute of the German Aerospace Center operates a research aircraft to create SAR images for external customers, DLR's internal research purposes as well as for testing new SAR techniques. The Do228-212 aircraft shown in Figure 1.2 serves as a platform for DLR's newest SAR system, called F-SAR. It provides fully polarimetric sensors in X-band, C-band, S-band, L-band and P-band with a resolution of up to 25 cm [3].

Figure 1.2: DLR's Do228-212 research aircraft with F-SAR system.

1.2 Ka-band PolInSAR

During the past few years, DLR's experience in the field of aircraft and satellite-based SAR systems has shown an increasing international interest in Ka-band SAR systems. Meanwhile, there is only limited experience worldwide in transfer of state-of-the-art SAR techniques into Ka-band. There is no known Ka-band SAR system with single pass interferometric or polarimetric capabilities. At the same time, more and more Ka-band hardware components become available for the commercial market. With the Ka-band PolInSAR Demonstrator, DLR intends to take the first big step towards aircraft-based Ka-band PolInSAR systems [4].

1.2.1 Ka-Band SAR Applications

Compared to existing SAR frequency bands, Ka-band has a significantly shorter wavelength and, therefore, is associated with lower penetration depth into volume. This physical property is of great advantage for some areas of application. For instance, the surface of snow on ice can be detected more precisely, which allows estimation of parameters such as the water equivalent of snow or the degree of snow coverage. The physical properties of Ka-band in combination with polarimetric and interferometric techniques extend the spectrum of applications in the field of climate research [4].

1.2.2 Requirements on the Antenna System

DLR's goal is building an airborne Ka-band SAR demonstrator system. The antenna system must combine the following requirements:

- The antenna has to be designed for a center frequency of 35.75 GHz. The bandwidth should be at least 500 MHz [4].
- The transmission power of the system requires low losses within the antenna system [4].
- The antenna system shall operate polarimetrically. Therefore, each antenna element must consist of a sub-antenna in horizontal and vertical polarization which must be located very close to each other due to the short wavelength of the system [4].
- The beamwidth of the antenna should be 30° in elevation and 5° in azimuth. The power should be bundled onto the swath and especially in nadir direction, as well as opposite swath direction the signal should be suppressed [4].
- At an altitude range of 0 m up to 6000 m, the military test standard described in Section 2.1.1 predicts a temperature range from 43 °C to –51 °C [1]. Since the maximum temperature of 43 °C is expected at sea level, this is not likely to occur during operation. Therefore, the temperature range of the antenna is rounded from 30 °C to –55 °C.

1.3 Motivation of this Work

With the development of a Ka-band PolInSAR system, DLR is facing a variety of new challenges. The higher frequency range as well as the implementation of state-of-the-art SAR techniques such as polarimetry and interferometry require complex antenna structures and thus new manufacturing methods such as plastic printing. The resulting use of new materials leads to a multitude of unknown properties.

In the practical report preceding this thesis, changes in the electrical parameters of a rectangular waveguide due to variations in temperature have been analyzed. The results have shown that changes in temperature mainly influence the signal phase and thus may influence the parameters of a slotted waveguide antenna. So far, neither simulations, nor measurements have been performed in this field. Furthermore, there is no measurement setup to investigate the behavior of an antenna in the required temperature range.

The objective of this thesis is to qualify a Ka-band plastic printed slotted waveguide antenna in the temperature range from 30 °C to –55 °C. The analysis is carried out both, theoretically, in form of simulations, and by measurement. A brass antenna of the same design serves as a reference for the plastic printed prototype. Both antennas were already tested at 21 °C in DLR's compact test range (CTR) and now the antenna parameters of both antennas shall be investigated under the influence of temperature. A further objective of this thesis is the development of a measurement setup to investigate the temperature behavior of antennas.

CHAPTER 2

THE SLOTTED WAVEGUIDE ANTENNA

This chapter provides theoretical background necessary for this thesis, including the altitude dependence of temperature, the theory of slots in a rectangular waveguide, the definition of spherical coordinate systems as well as the field regions surrounding an antenna. Further on, the slotted waveguide antennas investigated in this thesis are presented.

2.1 Theoretical Background

2.1.1 Altitude Dependent Temperature

In airborne SAR applications, the antenna is attached to the outside of the aircraft and exposed to extreme climatic conditions. Particularly, the temperature varies with flight altitude. The United States Military Standard MIL-STD-810G is a useful reference to determine the expected ambient temperatures and defines in METHODE 520.3 climatic conditions such as maximum and minimum temperature in dependence on the altitude. Table 2.1 shows these values up to an altitude of 6000 m [1].

Table 2.1: Maximum and minimum temperature for different flight altitudes [1].

Altitude	Min. temperature	Max. temperature
0 m	–51 °C	43 °C
1000 m	–49 °C	34 °C
2000 m	–31 °C	27 °C
4000 m	–40 °C	12 °C
6000 m	–51 °C	0 °C
8000 m	–61 °C	–11 °C
10000 m	–65 °C	–20 °C

2.1.2 Slotted Waveguide Antennas

In order to radiate an electromagnetic wave from a waveguide into free space, the structure must be opened. One way to decouple the electromagnetic wave is the open-ended waveguide, where the end of the waveguide is kept open. This single aperture which is small in relation to the wavelength, leads to a very wide beamwidth of the antenna. The aperture can be increased by a horn which in turn reduces the beamwidth. Depending on the geometric dimensions of this horn antenna, the energy of the signal can be focused with more or less intensity.

To define the radiation characteristics of the antenna more accurately, it is advisable to use several single radiators. By choosing the spacing of the radiators as well as defining their phase and amplitude, a complex antenna characteristic can be realized by the superposition of the individual radiated waves. This combination of several single radiators to a common antenna characteristic is called a "group antenna" and can be realized by introducing slots in the wall of a waveguide.

Radiating Slots

A narrow rectangular slot in a conducting surface radiates an electromagnetic field if it interrupts currents occurring in the surface with its long side, since these can be continued within the slot as a displacement current. If the currents are perpendicular to the long side, the intensity of the emitted electromagnetic wave is maximum and, if they occur parallel to the slot, the intensity is minimum. Furthermore, the intensity of the emitted electromagnetic wave can be defined by the strength of the current. As displacement currents are occurring parallel to the short side of the slot, the electric field and, therefore, the polarization of the electromagnetic wave is arranged perpendicular to the long side [5].

Surface Currents on a Waveguide

From the preliminary consideration of a single slot it follows that its orientation defines the polarization and the orientation in relation to the surface currents the intensity of the radiated wave. Therefore, it is essential to know the current distribution of a rectangular waveguide as shown in Figure 2.1 to design a slotted waveguide antenna.

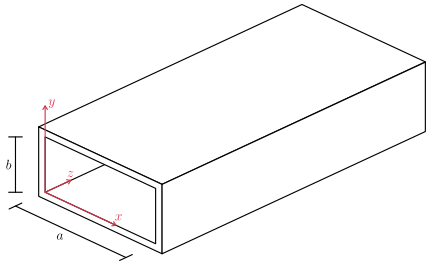

Figure 2.1: Rectangular waveguide with coordinate system.

The current density $\mathrm{J_F}$ can be calculated by using the boundary condition of the magnetic field at an ideally conducting surface as stated in Equation 2.1 [6] [7].

$$\mathrm{J}_F = \mathrm{n} \times \mathrm{H_t} \tag{2.1}$$

Thereby, n is the normal unit vector to the boundary layer and $\mathrm{H_t}$ the tangential magnetic field. For a TE_{mn} mode propagating in the rectangular waveguide, Pozar [8] gives the following equations for the longitudinal and transversal field components:

$$H_\mathrm{z}(x,y,z) = A_{mn} \cos\frac{m\pi x}{a} \cos\frac{n\pi y}{b} \mathrm{e}^{-\mathrm{j}\beta z} \quad , \tag{2.2a}$$

$$E_\mathrm{x} = \frac{\mathrm{j}\omega\mu n\pi}{k_\mathrm{c}^2 b} A_{mn} \cos\frac{m\pi x}{a} \sin\frac{n\pi y}{b} \mathrm{e}^{-\mathrm{j}\beta z} \quad , \tag{2.2b}$$

$$E_\mathrm{y} = \frac{-\mathrm{j}\omega\mu m\pi}{k_\mathrm{c}^2 a} A_{mn} \sin\frac{m\pi x}{a} \cos\frac{n\pi y}{b} \mathrm{e}^{-\mathrm{j}\beta z} \quad , \tag{2.2c}$$

$$H_\mathrm{x} = \frac{\mathrm{j}\beta m\pi}{k_\mathrm{c}^2 a} A_{mn} \sin\frac{m\pi x}{a} \cos\frac{n\pi y}{b} \mathrm{e}^{-\mathrm{j}\beta z} \quad , \tag{2.2d}$$

$$H_\mathrm{y} = \frac{\mathrm{j}\beta n\pi}{k_\mathrm{c}^2 b} A_{mn} \cos\frac{m\pi x}{a} \sin\frac{n\pi y}{b} \mathrm{e}^{-\mathrm{j}\beta z} \quad , \tag{2.2e}$$

where k_c is the cut-off wave number

$$k_\mathrm{c} = \sqrt{k^2 - \beta^2} \quad , \tag{2.3}$$

k is the wave number

$$k = \omega\sqrt{\mu\epsilon} \quad , \tag{2.4}$$

β the propagation constant

$$\beta = \sqrt{k^2 - \left(\frac{m\pi}{a}\right)^2 - \left(\frac{n\pi}{b}\right)^2} \tag{2.5}$$

and A_{mn} the amplitude constant. If only the TE_{10} mode is taken into account, the equations for the field components are reduced to:

$$H_\mathrm{z}(x,z) = A_{10}\cos\frac{\pi x}{a}e^{-\mathrm{j}\beta z} \tag{2.6a}$$

$$E_\mathrm{y} = \frac{-\mathrm{j}\omega\mu\pi}{k_\mathrm{c}^2 a}A_{10}\sin\frac{\pi x}{a}e^{-\mathrm{j}\beta z} \tag{2.6b}$$

$$H_\mathrm{x} = \frac{\mathrm{j}\beta\pi}{k_\mathrm{c}^2 a}A_{10}\sin\frac{m\pi x}{a}e^{-\mathrm{j}\beta z} \quad . \tag{2.6c}$$

Thus, the surface current density for the upper wall at $y = \mathrm{b}$ and the right-hand side wall at $x = 0$ can be calculated by the cross product of the unit vector perpendicular to the surface and the magnetic field component in z-direction [6]:

$$\mathrm{J}_\mathrm{F}^{top} = \mathrm{n}\times\mathrm{H} = -\mathrm{e}_\mathrm{y}\times\mathrm{H}_\mathrm{z} = A_{10}\left(\mathrm{e}_\mathrm{z}\frac{j\beta a}{\pi}\sin\frac{\pi x}{a} - \mathrm{e}_\mathrm{x}\cos\frac{\pi x}{a}\right)e^{-\mathrm{j}\beta z} \tag{2.7}$$

$$\mathrm{J}_\mathrm{F}^{side} = \mathrm{n}\times\mathrm{H} = -\mathrm{e}_\mathrm{x}\times\mathrm{H}_\mathrm{z} = \mathrm{e}_\mathrm{y}A_{10}e^{-\mathrm{j}\beta z} \quad . \tag{2.8}$$

This results in surface currents shown in Figure 2.2 which also shows possible arrangements of slots in waveguide walls. Slots aligned with the direction of current such as slots b) and g) do not radiate an electromagnetic wave since their long side is parallel to surface currents. All other slots are perpendicular to surface currents so that they radiate. With respect to the horizontal plane indicated in the graphic, all slots on the broad wall a), b), c), d) and the longitudinal slot on the narrow side e) radiate a vertically polarized field. The inclined slot on the narrow side radiates an electric field rotated by 45° to the horizontal plane, while slot g) would be horizontally polarized if it radiated.

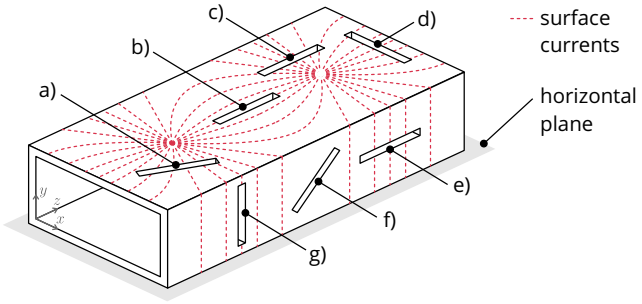

Figure 2.2: Surface currents on a rectangular waveguide with a) inclined slot on broad wall, b) and c) longitudinal slots in broad wall, d) transversal slot in broad wall, e) longitudinal slot in narrow wall, f) inclined slot in narrow wall, g) transversal slot in narrow wall.

Vertically Polarized Slotted Waveguide Antennas

A common way to create a vertically polarized slotted waveguide antenna is to insert several longitudinal slots on the broadside of the waveguide. When choosing a resonant design the waveguide end is terminated with a wall which forms a short-circuit and results in a standing wave. The slots are placed alternately on the broadside at a distance from the centerline. Due to alternating arrangement and the associated change in sign, they can be placed at a distance of half the guided wavelength λ_G, whereby the distance of the last slot to end wall is $\lambda_G/4$ [9].

The intensity of the emitted electromagnetic wave of each slot is dependent of its distance to the centerline. If all slots are uniformly arranged, the main lobe is the narrowest, but the side lobes are quite high. Side lobes can be reduced by different distance to centerline, which leads to a different amplitude allocation. Amplitude assignments according to binomial coefficients or Chebyshev polynomials are common [6].

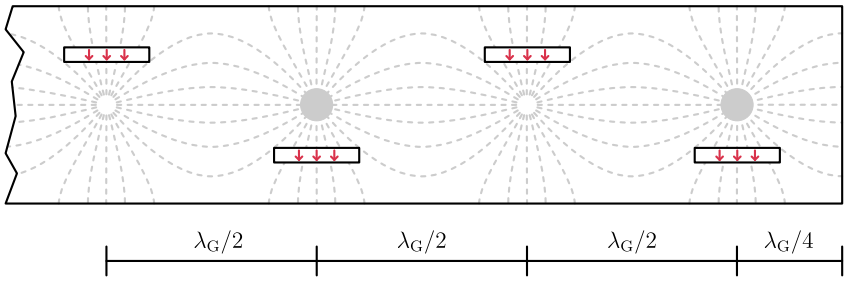

Figure 2.3: Longitudinal slots on the broad wall of a rectangular waveguide.

Horizontally Polarized Slotted Waveguide Antennas

Creating a horizontally polarized slotted waveguide antenna is a challenge. With a standard waveguide, the creation of a horizontal polarization is only possible by alternating the inclinations of a narrow wall inclined slot. This allows to place the slots in a distance of $\lambda_G/2$. By the superposition of the single radiators' field a common horizontally polarized field is created. However, this is associated with a usually undesired high cross-polarization component [10].

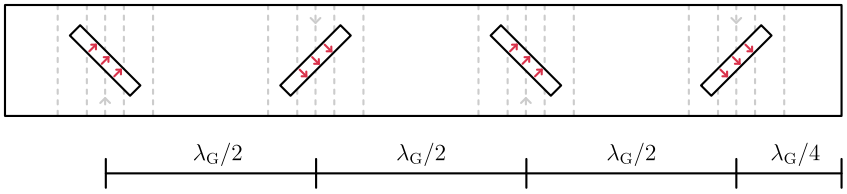

Figure 2.4: Inclined slots on the narrow wall of a rectangular waveguide.

Also the use of a transverse slot on the broad wall and the subsequent tilting of the waveguide to force the horizontal polarization does not lead to a satisfactory result since the slots have to be placed at a distance of λ_G and thus, grating lobes are exited.

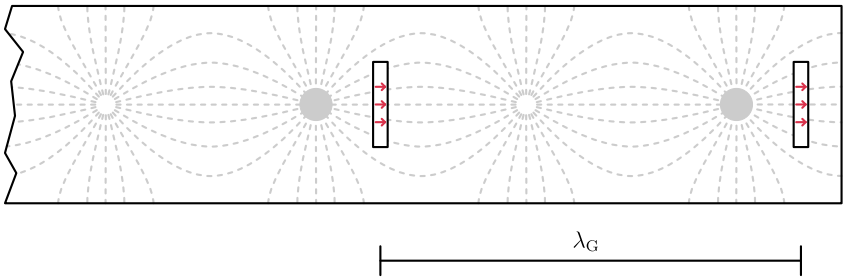

Figure 2.5: Transversal slots on the broadside wall of a rectangular waveguide.

An optimal slot for horizontally polarized slotted waveguide with lowest cross-polarization component is one in transverse direction on the narrow side. However, as this does not interrupt the surface currents in the waveguide walls and, therefore, does not radiate, the surface currents on the waveguide walls have to be modified. This can be achieved by introducing several iris structures into the waveguide as shown in Figure 2.6. An appropriate dimensioning of the iris structure with transverse slots leads to a horizontally polarized antenna with lowest cross-polarization component [11].

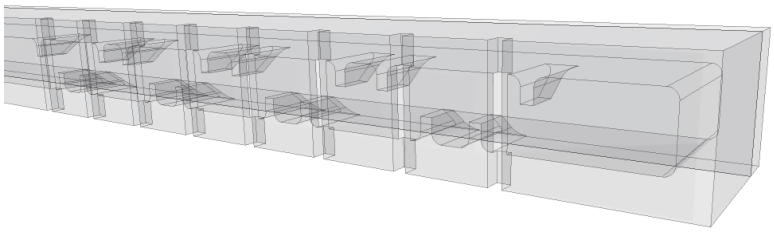

Figure 2.6: Iris structures inside a waveguide with transversal slots on the narrow wall.

2.1.3 Coordinate Systems

To describe antenna characteristics, a unique reference system is necessary. In this thesis the coordinate system shown in Figure 2.7a is used to relate the simulation and measurement results with the environment. The azimuth-elevation (az-el) positioning system shown in Figure 2.7b is used to define the position of the antenna within this environment.

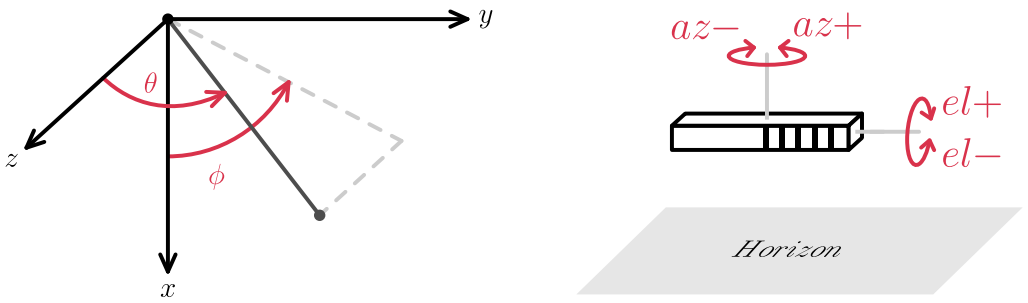

(a) (b)

Figure 2.7: Spherical coordinate system (a) and elevation over azimuth positioning system (b).

In the further course of this thesis, the terms co- and cross-polarization are used. A measurement or simulation in co-polarization is equal to the polarization primarily radiated by the object, whereas the cross-polarization is perpendicular to it.

2.1.4 Antenna Field Regions

Considering the field in direct proximity to the antenna, it can be seen that the distribution of the electromagnetic field differs from that in a certain distance to the antenna. The area around an antenna can be divided into three regions, whereas the

distance R to the antenna can be calculated by the maximum size of the aperture D and the free space wavelength λ [12]:

Reactive near-field region is the area directly surrounding the antenna in which the field begins to propagate. A strong interaction within the electromagnetic field takes place, while the field is superimposed with non-radiating field components. This region extends up to a distance of

$$R < 0.62\sqrt{\frac{D^3}{\lambda}} \quad . \tag{2.9}$$

Radiating near-field region, also called Fresnel region, is the area between reactive near field and far field. When emitting an electromagnetic wave from an aperture, a phase error occur due to the different distances from the point of observation to the individual locations on the aperture. This phase error increases with the size of the aperture and decreases with the distance to the antenna. The radiating near-field region is defined as the region in which this phase error is always less than $\pi/8$. Since this error depends on the size of the aperture, it can be omitted for antennas with small dimensions. It starts at a distance of

$$R \geq 0.62\sqrt{\frac{D^3}{\lambda}} \tag{2.10}$$

and ends at

$$R \leq \frac{2D^2}{\lambda} \quad . \tag{2.11}$$

Far-field, also called Fraunhofer region, is the area in which the angular field distribution is independent of the distance to the antenna. It starts from a distance of

$$R > \frac{2D^2}{\lambda} \quad . \tag{2.12}$$

2.2 Antenna Prototype

The Ka-band PolInSAR system will consist of multiple antennas arranged in an array to enable features such as beam forming. The beam of the antenna in elevation has to be adaptable, whereas it always remains the same in azimuth. Therefore, the

characteristics of the antenna in azimuth can already be realized by the characteristics of the single element of the array.

In the antenna array, a horizontally and a vertically polarized antenna element are alternated, whereby the distance between two identical polarizations must be as small as possible to avoid grating lobes. This leads to a very low thickness of the material, which is, similar to the iris structure inside the horizontally polarized waveguide, difficult to manufacture with classical milling technologies. A single element of this array consists of 16 slots and is fed centrally from the backside.

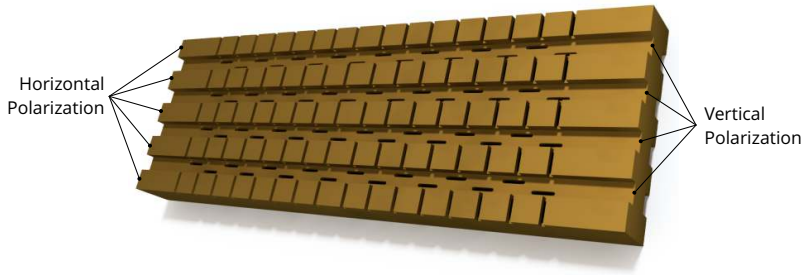

Figure 2.8: Array of horizontally and vertically polarized slotted waveguide antennas.

To study the technology of the single element, prototypes were produced in horizontal and vertical polarization. It represents half of a single element of the antenna array and is fed from the side. The vertical polarization was realized by longitudinal slots on the broadside of the waveguide. The horizontal polarization, on the other hand, was achieved by transversal slots on the narrow side and the use of internal iris structures as introduced in Section 2.1.2 and shown in Figure 2.6.

In particular the horizontally polarized slotted waveguide antenna places high demands on the manufacturing techniques which can be fulfilled by additive manufacturing methods. Two prototypes of the horizontally polarized antenna were produced. The first one was conventionally milled from brass and, where the antenna body was divided into two elements, which were soldered together afterwards. The second one was manufactured by SWISSto12 SA using a 3D printing method. The antenna consists of a coherent plastic element which was metallized with a layer of copper.

Figure 2.9: Antenna prototypes made of brass (left) and plastic (right).

The investigation of these antennas is the focus of this thesis. From this point on it is commonly referred to the antenna prototypes as antenna under test (AUT).

Material Overview

In the following the material properties of the brass and plastic antenna prototypes are introduced.

Table 2.2: Material properties of the copper clad plastic printed slotted waveguide antenna.

Parameter	Unit	Value	Condition	Reference
Designation of the plastic		Material M	*SWISSto12 SA* internal designation	[13]
Designation of the metallization		copper		[13]
Coefficient of thermal expansion of the plastic	K^{-1}	$53.0 \cdot 10^{-6}$	horizontal printing direction from 0 °C to 60 °C	[13]
		$56.0 \cdot 10^{-6}$	vertical printing direction from 0 °C to 60 °C	
		$28.0 \cdot 10^{-6}$	horizontal printing direction at −70 °C	
		$23.5 \cdot 10^{-6}$	vertical printing direction at −70 °C	
Coefficient of thermal expansion of the metallization	K^{-1}	$16.0 \cdot 10^{-6}$		[13]
Electrical conductivity	$S\ m^{-1}$	$58.8 \cdot 10^{6}$	at 20 °C	[14]
Electrical resistance	Ω m	$17.0 \cdot 10^{-9}$	at 20 °C	[14]
Temperature coefficient of electrical resistance	K^{-1}	$3.93 \cdot 10^{-3}$	at 20 °C	[14]
Thickness of the metallization	m	$5 \cdot 10^{-6}$		

Table 2.3: Material properties of the brass milled slotted waveguide antenna.

Parameter	Unit	Value	Condition	Reference
ISO designation		CuZn39Pb3		
Coefficient of thermal expansion	K^{-1}	$19.3 \cdot 10^{-6}$	from 20 °C to 100 °C	[15]
Electrical conductivity	S m^{-1}	$15.0 \cdot 10^{6}$	at 20 °C	[15]
Electrical resistance	Ω m	$66.0 \cdot 10^{-9}$	at 20 °C	[15]
Temperature coefficient of electrical resistance	K^{-1}	$1.7 \cdot 10^{-3}$	at 20 °C	[15]
Magnetic permeability		1	at 20 °C	[15]

CHAPTER 3

THEORETICAL INVESTIGATION OF THE SLOTTED WAVEGUIDE ANTENNA

This chapter deals with the simulation of antennas under the influence of temperature. The preceding practical report to this thesis has shown that temperature, on the one hand, has the greatest influence on a waveguide due to thermal expansion which causes a shift in signal phase. On the other hand, the variation of the electrical conductivity over temperature has less influence on a waveguide. The conductivity of the materials copper and brass differs much more than the difference occurring due to changes in temperature [16].

Due to variations in signal phase or amplitude within the slotted waveguide, the phase and amplitude assignment of the slots changes as well and leads to a change in the antenna characteristic. To estimate the impact of this effect, the antenna is simulated with extreme values for length and conductivity in the first place. Thereafter, both the plastic and brass antenna are simulated with realistic values on their behavior at different temperatures. All simulations are performed with the field simulation software Ansys HFSS.

3.1 Simulation Model

The computer model to simulate the influences of temperature on the characteristic of the antenna is based on the model from the development of the slotted waveguide antenna. It mainly consists of the antenna structure which is placed in a vacuum body to distinguish it from the perfectly conductive workspace in HFSS and enable the propagation of electromagnetic waves. The distance from the antenna to the vacuum body is at least $\lambda/4$. A perfect matched layer is placed at the border between vacuum box and the perfect conducting environment to prevent the reflection of electromagnetic waves and enable the calculation of the radiation pattern. The excitation of the electromagnetic wave inside the waveguide is realized by a wave port which provides an ideal TE_{10} mode. The model is made fully parameterizable

to provide unrestricted access to all dimensions of the model which must change depending on a temperature variable in order to simulate the thermal expansion of the antenna. The calculation of the length as a function of temperature difference is carried out via the coefficient of thermal expansion (CTE) according to Equation 3.1, where α represents the CTE, L_0 the length of the object at reference temperature and ΔT the temperature difference [14].

$$L(\Delta T) = L_0(1 + \alpha \cdot \Delta T) \tag{3.1}$$

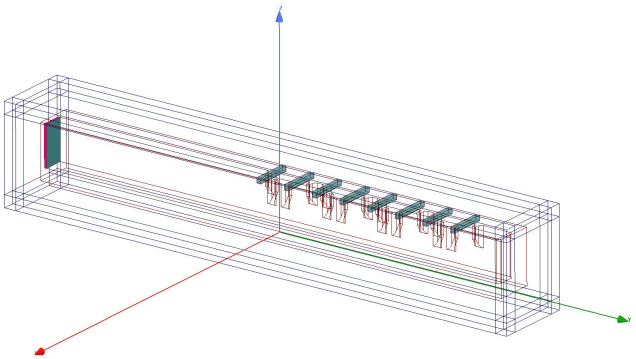

Figure 3.1: HFSS simulation model of the slotted waveguide antenna.

3.2 Separate Investigation of Influences

In the first step of investigation, the change of conductivity and change due to thermal expansion are investigated separately.

3.2.1 Change in Electrical Conductivity

In the following, the influence of conductivity on the input reflection coefficient as well as the radiation pattern of the antenna is investigated. The electrical conductivity is defined by the material properties of the HFSS antenna model. It can also be equipped with a thermal modifier, thus, the change of conductivity can be adjusted depending on temperature. Since the change in conductivity within the temperature limit is smaller than the difference in conductivity between both materials independent of temperature, both materials are investigated without using a thermal modifier. Thereby, brass has a conductivity of $15.0 \cdot 10^6$ S m^{-1} and plastic of $58.8 \cdot 10^6$ S m^{-1} which corresponds to the conductivity of the metallization. Both antennas are assumed to be made of a solid material since the thickness of metal-

lization is greater than the skin depth and can, therefore, be neglected as described in the practical report preceding this thesis [16].

In both, the simulation of the input reflection coefficient and antenna gain, only slight differences between the materials can be detected. The input reflection coefficient of the copper antenna is degraded slightly, whereas the antenna gain in horizontal polarization does not change and differs slightly between both materials in vertical polarization.

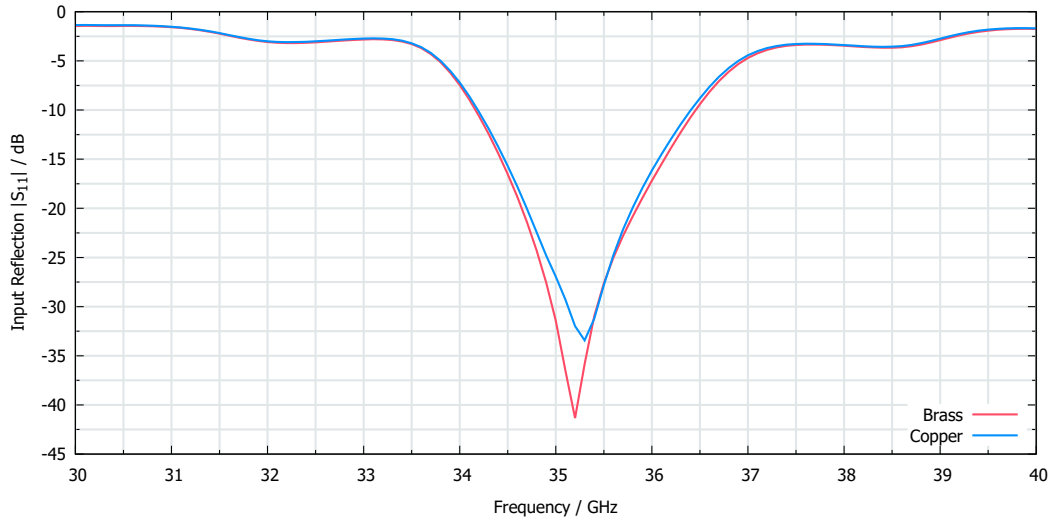

Figure 3.2: Simulation of the input reflection coefficient of two antenna models with different conductivities.

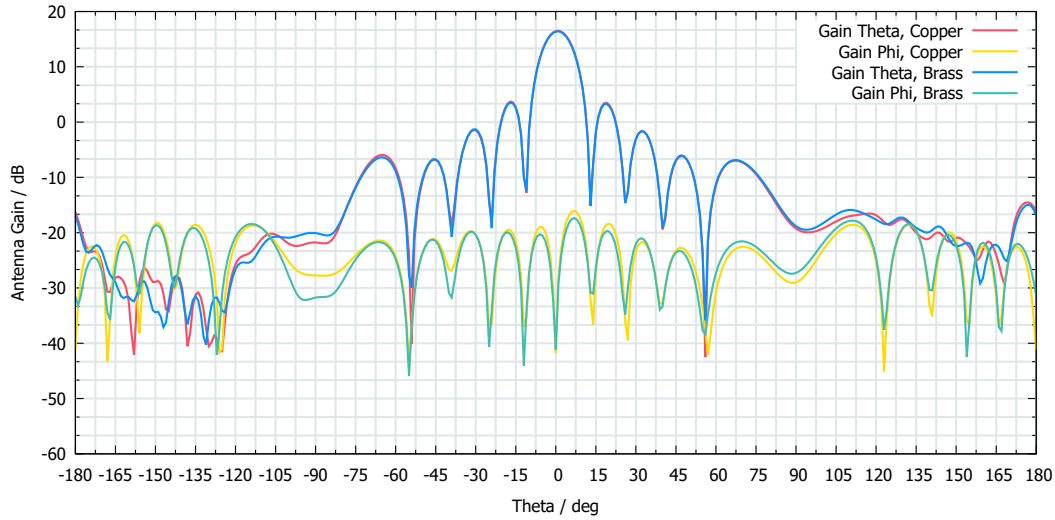

Figure 3.3: Simulation of the antenna gain of two antenna models with different conductivities. Gain theta is simulated at an 0° elevation, gain phi at 20° elevation.

3.2.2 Thermal Expansion

In this section, the antenna is simulated with a coefficient of thermal expansion of $0.5 \cdot 10^{-3}$ K^{-1}, which is approximately 10 times higher than the CTE of plastic in order to make influence of thermal expansion clearly visible. The temperature difference is set to 100 K. At this strong thermal expansion a clear difference in the input reflection coefficient (Figure 3.4) as well as in the antenna gain (Figure 3.5) is visible. The minimum of the input reflection coefficient shifts significantly towards higher frequencies at low temperatures and the antenna gain shows a strong change in pattern.

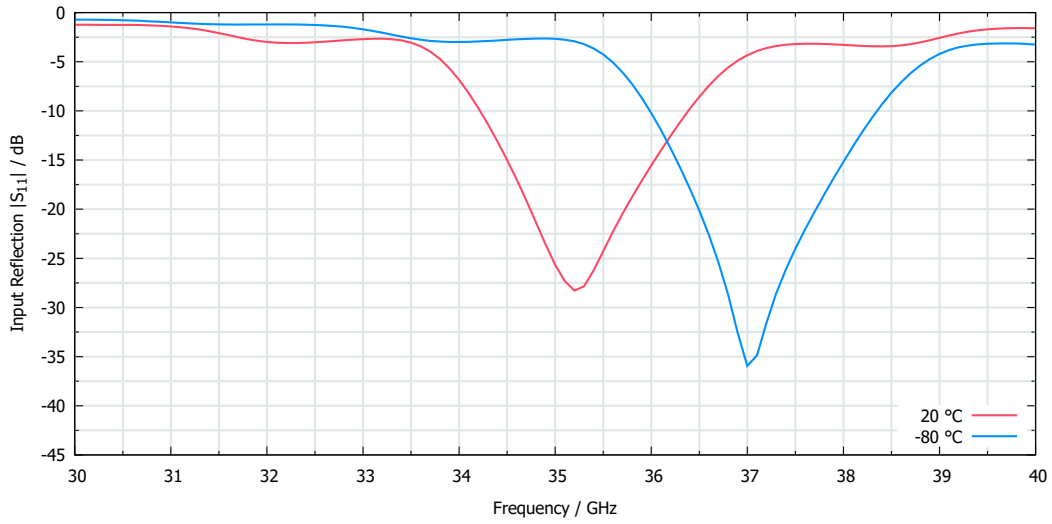

Figure 3.4: Simulation of the input reflection coefficient for extreme changes in length.

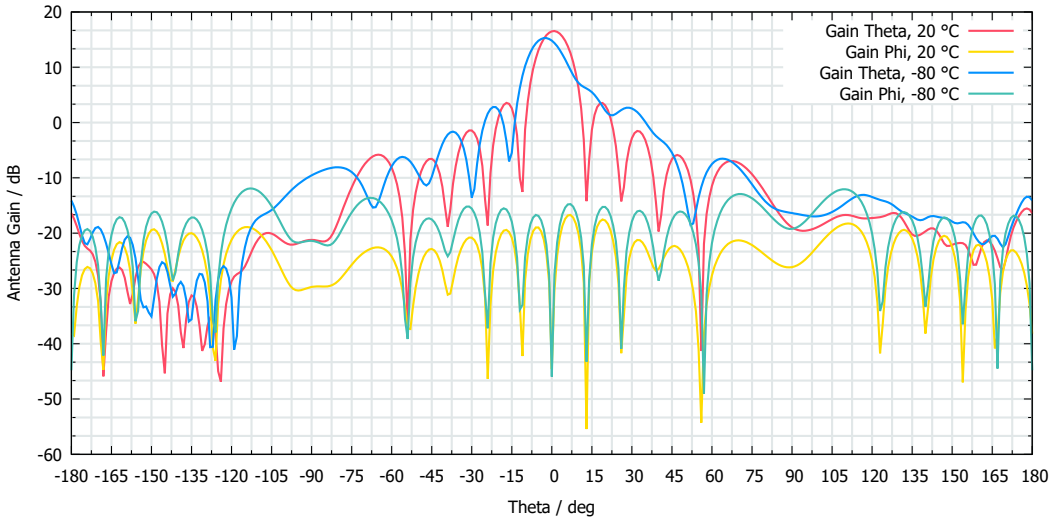

Figure 3.5: Simulation of the antenna gain for extreme changes in length. Gain theta is simulated at an 0° elevation, gain phi at 20° elevation.

3.3 Simulation of the Existing Antennas

Whereas the general influence of thermal expansion and conductivity was investigated in the previous section, in this section, the antenna is simulated with its actual parameters as listed in Table 3.1. The coefficient thermal expansion as well as the thermal dependence of the conductivity is examined. The simulation is carried out at the temperature limits of 30 °C and –40 °C.

Table 3.1: Material parameters used in simulation.

Parameter	Unit	Brass antenna	Plastic antenna
Coefficient of thermal expansion	K^{-1}	$19.3 \cdot 10^{-6}$	$53.0 \cdot 10^{-6}$
Electric conductivity	S m^{-1}	$15.0 \cdot 10^{6}$	$58.8 \cdot 10^{6}$
Temperature coefficient of electrical resistance	K^{-1}	$1.7 \cdot 10^{-3}$	$3.93 \cdot 10^{-3}$

3.4 Simulation Results

The following section examines the simulation results of the input reflection coefficient and antenna gain using actual material parameters of brass and plastic.

3.4.1 Input Reflection

The minimum of the input reflection coefficient of the brass and plastic antenna is shifted as expected towards high frequencies at lower temperatures. The notch in the input reflection coefficient of the brass antenna shifts by approximately 70 MHz. In case of the plastic printed antenna, this shift is about 170 MHz due to the higher coefficient of thermal expansion.

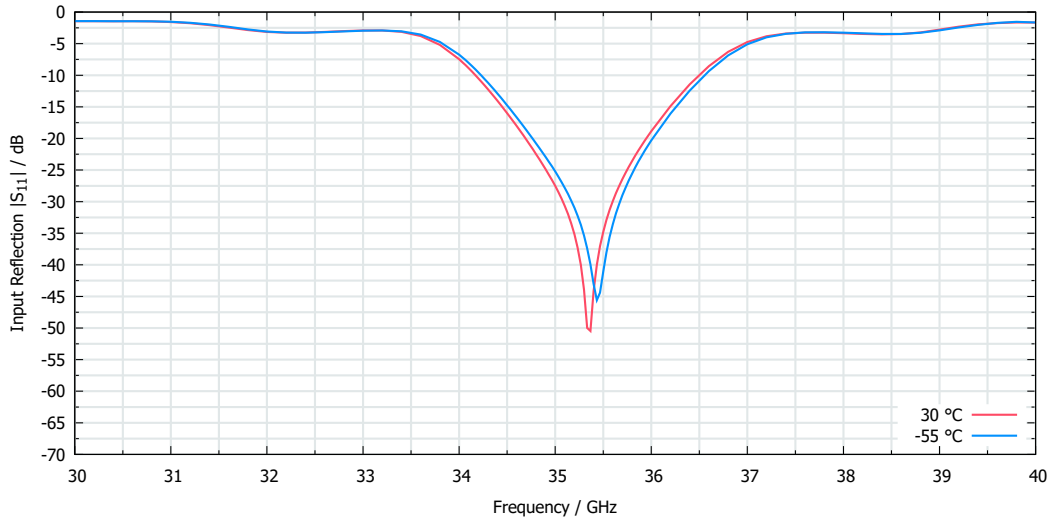

Figure 3.6: Simulation of the input reflection coefficient of the brass antenna at the temperature limits by taking into account the change in conductivity and change in length.

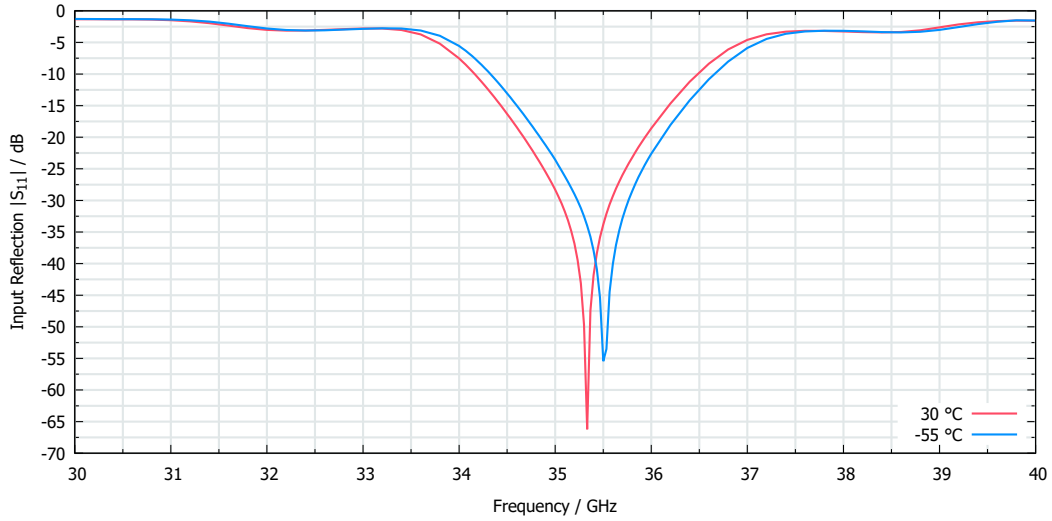

Figure 3.7: Simulation of the input reflection coefficient of the plastic printed antenna at the temperature limits by taking into account the change in conductivity and change in length.

3.4.2 Antenna Gain

The antenna gain experiences only a very small variation due to a change in temperature as shown in Figure 3.8 and 3.9. The antenna characteristic shows a very slight shift towards a negative theta angle at lower temperature. This effect is shown in Figure 3.10 and is least in area of the main lobe and slightly greater with plastic than with the brass antenna.

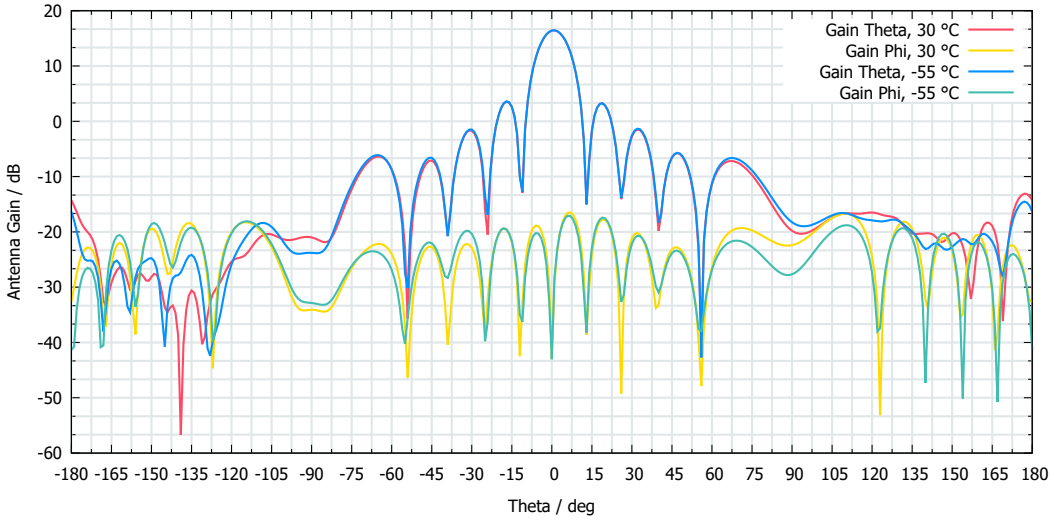

Figure 3.8: Simulation of the antenna gain of the brass antenna at the temperature limits by taking into account the change in conductivity and change in length. Gain theta is simulated at an 0° elevation, gain phi at 20° elevation.

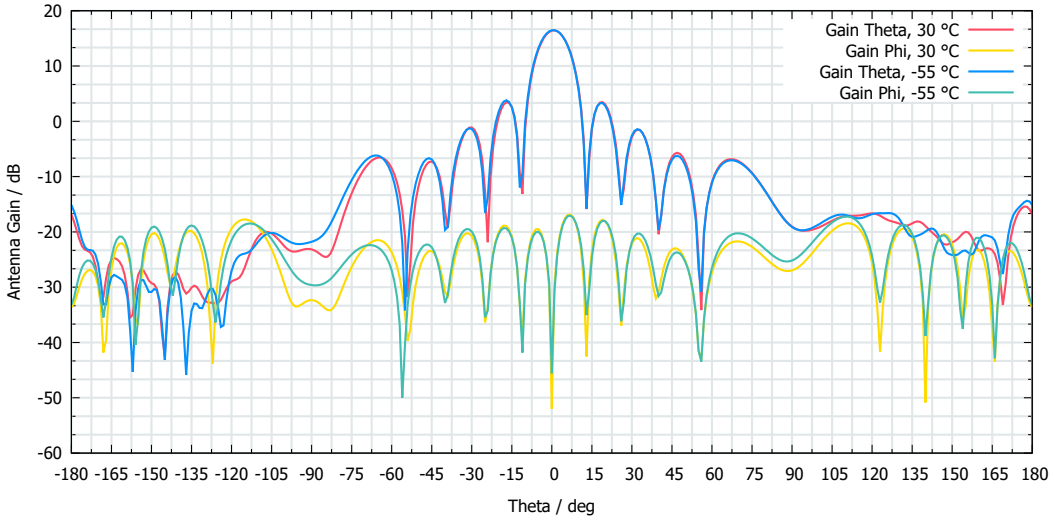

Figure 3.9: Simulation of the antenna gain of the plastic printed antenna at the temperature limits by taking into account the change in conductivity and change in length. Gain theta is simulated at an 0° elevation, gain phi at 20° elevation.

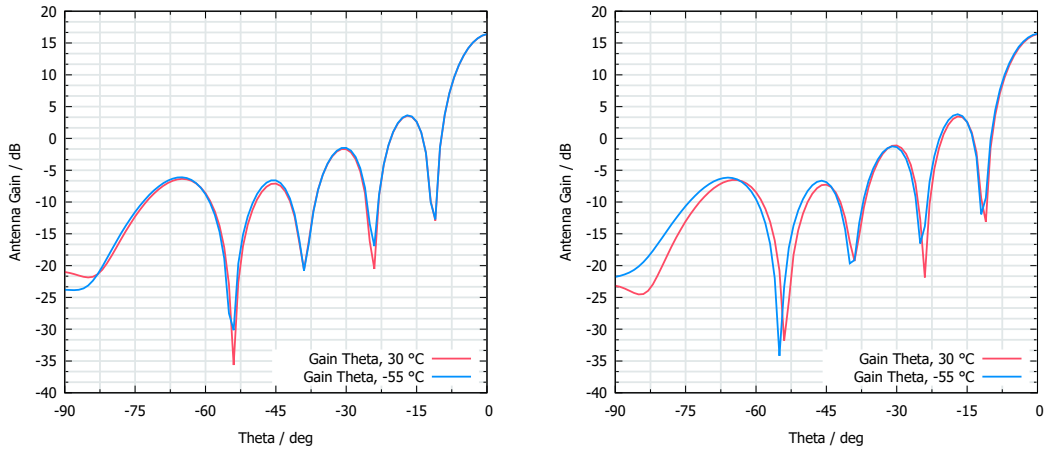

(a) (b)

Figure 3.10: Detail view of the simulated antenna gain of the brass (a) and the plastic printed antenna (b) at the temperature limits by taking the change in conductivity and change in length into account. Gain theta is simulated at an 0° elevation.

CHAPTER 4

MEASUREMENT OF THE SLOTTED WAVEGUIDE ANTENNA

This chapter covers the practical examination of the antennas. It describes the design of a measurement setup to determine the change of antenna characteristic occurring over temperature and presents the raw measurement data.

The aim of the measurement is to verify the simulation results, whereas determining exact antenna parameters, such as antenna gain, are not an aim of this thesis. Each antenna is measured at different temperatures to detect changes in antenna characteristic due to comparison of scattering parameters.

4.1 Development of the Measurement Setup

The following section describes the various aspects that have to be considered in order to design a suitable measurement setup for qualifying the antenna in the desired temperature range. A detailed listing of the used measurement equipment can be found in the appendix Chapter A.

4.1.1 Method to Reach Operating Temperature

In order to characterize the antenna in operating temperature range and to verify the simulation results, it is necessary to find a way keeping the antenna at a constant temperature during the measurement. A wide temperature range from 30 °C to –55 °C has to be covered. Among the available means, the temperature chamber is the instrument of choice for this purpose, as it offers thermal accuracy, time stability and sufficient homogeneous temperature control of the object under test. Nevertheless, the use of a temperature chamber complicates the measurement of the antenna.

Due to the physical dimensions of the measurement setup, it is not possible to place both the AUT and probe antenna inside the temperature chamber. On the one hand, this arrangement is advantageous, as the thermal changes only affect the AUT and its supply cable without influencing the rest of the measurement setup. On the other hand, the metallic enclosure of the temperature chamber prohibits measurement of the antenna characteristic from the outside. A possibility has to be found to perform measurements while the door of the temperature chamber remains open without influencing the temperature of the test object. Moreover, the metallic housing leads to reflections of the radiated signal and thus, to distortion of measurement results.

The used temperature chamber enables thermal conditioning in the range from 180 °C to –40 °C. Thus, the lower limit of operating temperature range of the antenna cannot be reached. Nevertheless, it is possible to achieve the occurring temperature difference of 85 K by shifting the upper temperature limit by 15 K up to 45 °C. The temperature chamber does not support the variation of further climate parameters such as humidity or pressure.

4.1.2 Temperature Chamber Door Replacement

A replacement for the chamber door, which does not influence the electromagnetic signal of the antenna and thermically insulates the inside of the chamber from the environment, is required in order to facilitate measuring the radiated field of the antenna inside the temperature chamber. A 80 mm polystyrene insulation panel is used for this purpose. To ensure that the polystyrene panel has no influence on the measurement, the forward transmission coefficient is measured before and after the use of the insulation panel.

Due to the zeros in radiation pattern of the slotted waveguide antenna, the influence of polystyrene can not be determined exactly. Therefore, a Ka-band horn antenna is used to investigate the forward transmission of the measurement setup. The horn antenna is placed inside the climatic chamber and with the probe antenna, introduced later in this chapter, the transfer function at different incident angles is measured. A linear axis, which is also introduced later, is used for positioning the probe antenna.

The investigation shows that the polystyrene panel does not cause a significant difference in signal amplitude in the theta range from –20° to 20°. Outside this range, the sensitivity of the measurement setup is not sufficient to draw a conclusion, due to the low signal amplitude of the horn antenna at these angles and the multiple

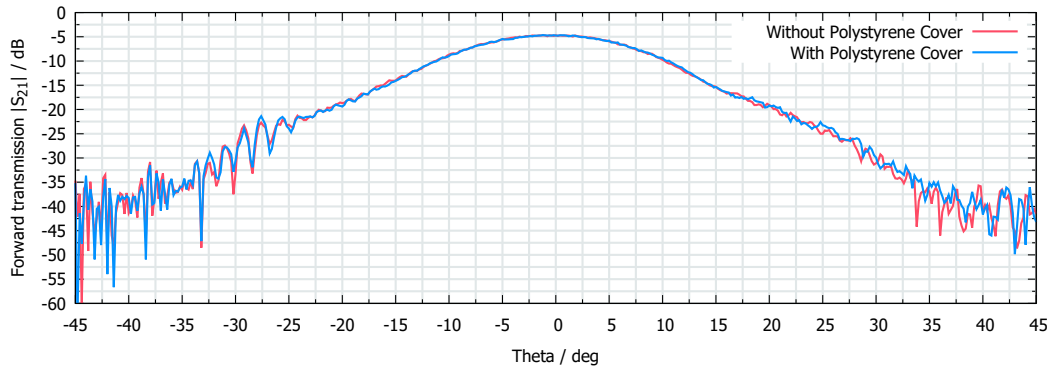

Figure 4.1: Forward transmission coefficient of the measurement setup with and without the polystyrene panel.

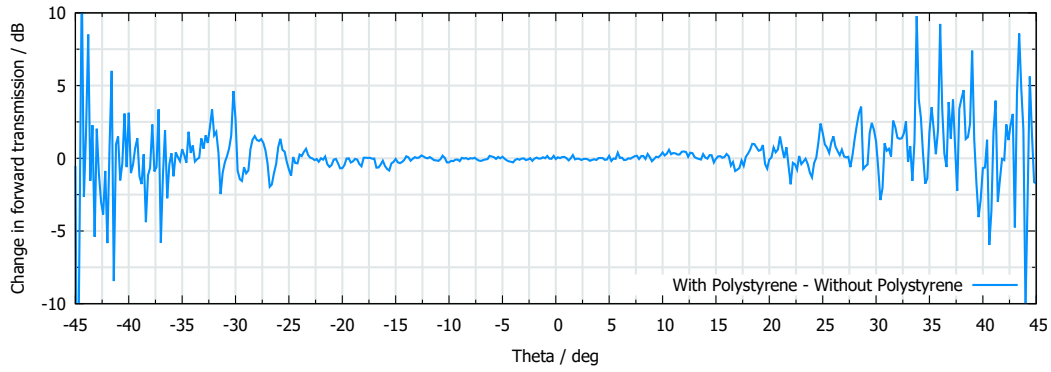

Figure 4.2: Difference in forward transmission of the measurement setup with and without the polystyrene panel

reflections that occur on metallic surfaces in the measurement setup. Since the insulating panel has the same influence on the results of all measurements and therefore the comparison of the measurement results at different temperatures is not affected, the polystyrene panel is suitable as a door replacement.

4.1.3 Reduction of Reflections within Temperature Chamber

As the temperature chamber is internally enclosed with metal, reflections on the inside walls and thus, multipath propagation of the signal are expected. In order to minimize this undesired effect, the temperature chamber is covered on the inside with radiation absorbent material (RAM). While a pyramidal shaped RAM is used on the back of the climatic chamber, a plate shaped RAM is used on the top, bottom and sides due to the limited distance to the AUT.

In order to analyze the influence of multipath propagation, the forward transmission of the measurement setup is measured before and after the use of RAM. The

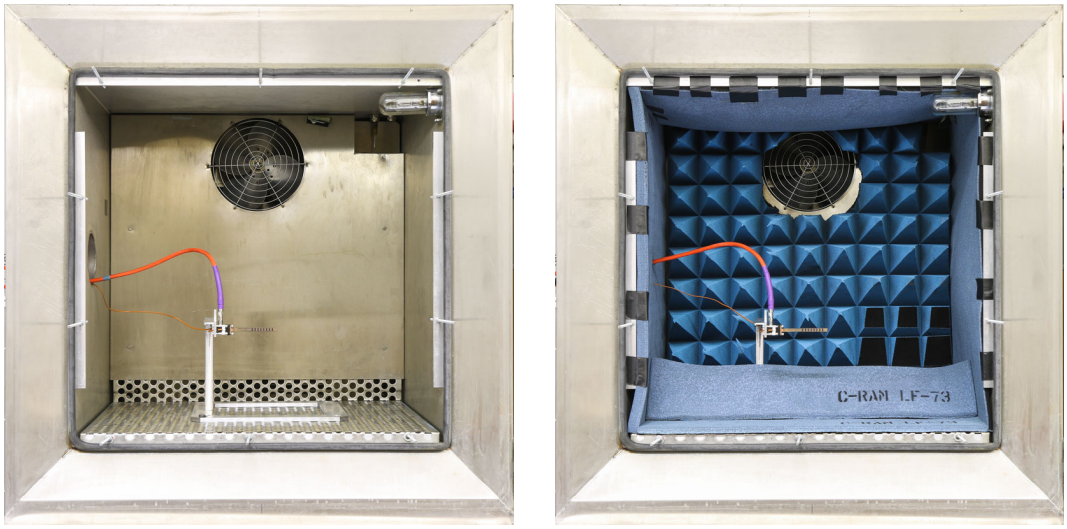

(a) (b)

Figure 4.3: Inside of the temperature chamber without radiation absorbent material (a) and with the inside of enclosure covered with radiation absorbent material (b).

measurements clearly show a reduction in ripple of the signal as shown in Figure 4.4. Noise was assumed to be the cause of the remaining ripple of the signal, but this could be excluded, as the noise floor was detected far beyond the measured signal when the antenna was shielded. The remaining ripple of the signal is due to residual reflected signals. These can occur, for instance, on the metallic front of the temperature chamber or on other surfaces within the measurement setup. However, further use of RAM is avoided due to high associated costs.

4.1.4 Prevention of Icing

One effect that must be considered while cooling down the temperature chamber is condensation. If air cools down, its relative humidity increases and when a saturation of 100% is reached, the water condenses [17]. If the humidity condenses at the surface or inside the slotted waveguide antenna, this probably will distort the measurement.

One attempt to prevent this, was to displace the air by nitrogen which can be achieved by placing liquid nitrogen inside the temperature chamber. According to the product datasheet of the liquid nitrogen, 1 liter of liquid nitrogen at boiling temperature of –195.8 °C produces 691 liter of nitrogen gas at 15 °C [18]. Assuming a volume of the temperature chamber of about 350 liters, 1 liter of liquid nitrogen shall suppress most of the air inside the chamber during the cooling process and prevent condensation at the antenna.

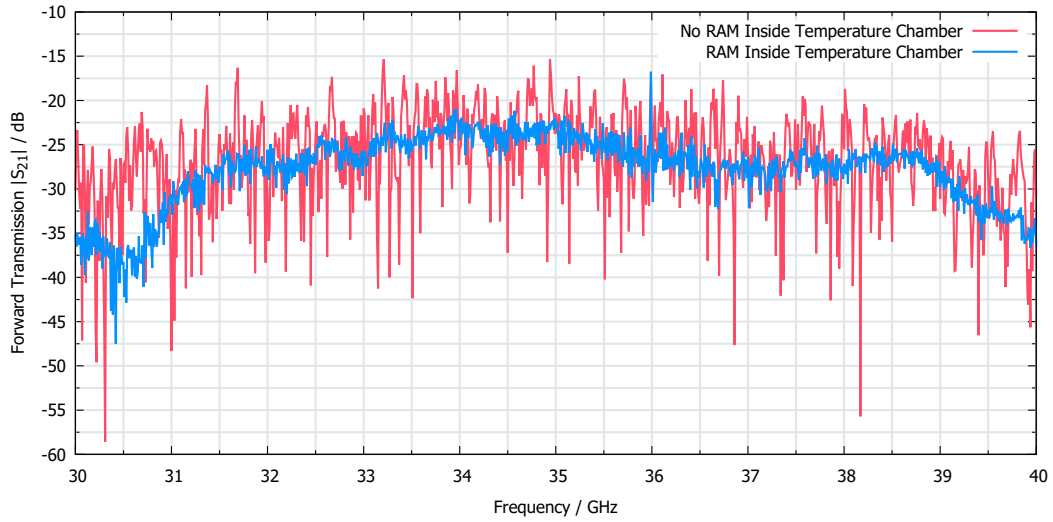

Figure 4.4: Reduction of reflections within the temperature chamber by using radiation absorbent material. The measurement is performed with the brass slotted waveguide antenna at 0° elevation and 0° theta.

However, the measurement shows that liquid nitrogen has an influence on the forward transmission of the measurement setup. Figure 4.5 shows the forward transmission over time, whereby after 15 min the liquid nitrogen was added into a jar inside the climatic chamber. From this moment on, the forward transmission coefficient increases. The cause of this effect could not be clarified in course of this thesis. Since the concentration of nitrogen cannot be controlled during the measurement, it is not used for this purpose.

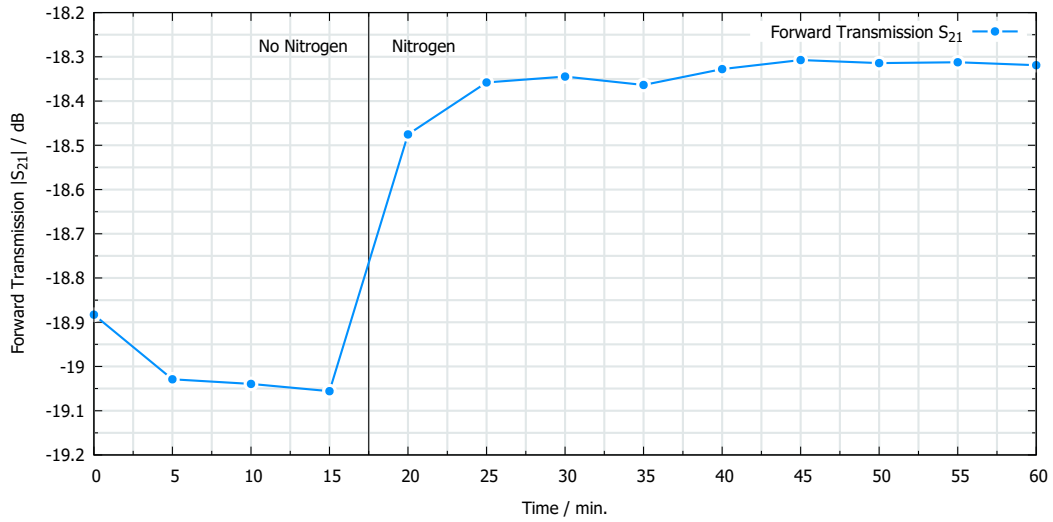

Figure 4.5: Change in forward transmission upon addition of liquid nitrogen at 15 min $< t <$ 20 min.

Cooling the temperature chamber and opening the door at –40 °C shows that there is no icing visible on the AUT. Thus, humidity seems to condense during the cooling process at the coldest point in the system, namely the air conditioner. The antenna, on the other hand, will remain free from condensation and icing if no warmer air flows into the system. By keeping the temperature chamber cover closed during the entire measurement, a sufficient minimization of condensation effects seems to take place.

4.1.5 Selecting the Probe Antenna

The probe antenna serves the purpose to measure the signal radiated from the AUT at a certain point in space. Since this antenna shall move alongside a linear axis parallel to the slotted waveguide antenna without correcting the angle in relation to the AUT, it must exhibit a broad main lobe to minimize the error occurring at wide incident angles. In general, it can be stated that the smaller the aperture of an antenna, the larger is its beamwidth. For this reason a small horn antenna, very similar to an open-ended waveguide, is selected.

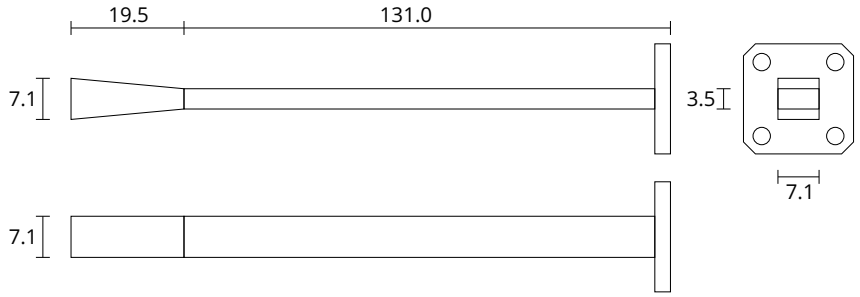

Figure 4.6: Dimensions of the horn probe antenna.

The antenna is simulated with HFSS since the manufacturer of the probe antenna is unknown and no measurement data is available. Figure 4.7 illustrates the wide main lobe of the antenna which in general enables a linear scan of an object, while neglecting a certain error in amplitude but also leads to receiving numerous unwanted signals caused by multipath propagation.

The antenna is vertically polarized at $\phi = 0°$ which means that the cross-polarization component of the AUT is measured. To perform measurements in co-polarization, the probe antenna is twistet to $\phi = 90°$. In order to determine which amplitude error the antenna causes in co- and cross-polarization over the scan angle, the antenna must be examined at both installation angles. Figures 4.8 shows the simulation of the co- and cross-polarization components at both installation positions. Figure 4.8a and 4.8b show that the amplitude decreases with increasing incidence angle of the

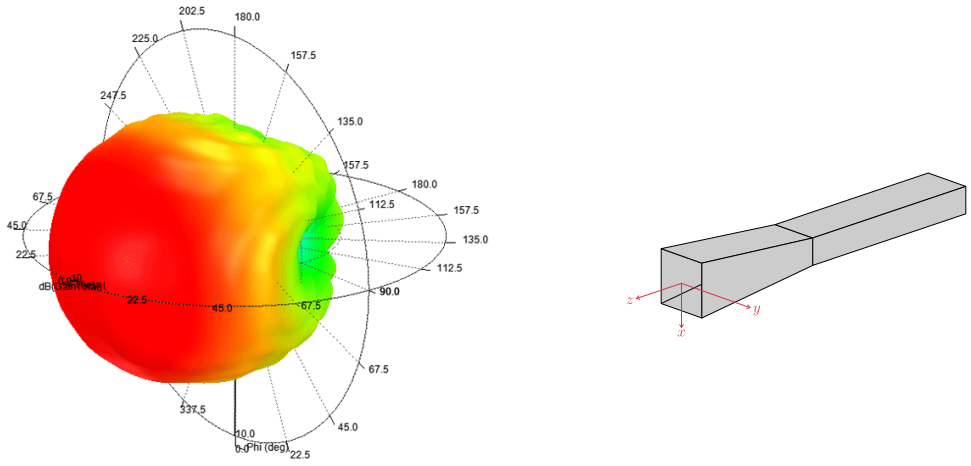

(a) (b)

Figure 4.7: 3D antenna gain plot of the probe horn antenna (a) and corresponding alignment of the antenna (b).

wave. The decreased amplitude at high incidence angles leads to an uneven evaluation of the amplitude at different angles. In addition, it must be ensured that the signal is not attenuated beyond the sensitivity of the measurement setup.

The simulation shows, that in the desired angle range from –45° to 45°, a reduction of the amplitude at high incidence angles by approximately 10 dB is expected. The further design of the measurement setup shows that there is still sufficient signal-to-noise ratio to detect weak signals, for instance in cross-polarization. Furthermore, the unequal evaluation of the amplitude as a function of theta remains the same for each measurement. The simulation shows a suppression of the cross-polarization of about 30 dB, whereby, during measurement of the vertical polarization of the AUT, the horizontally radiated signal should be sufficiently isolated. Therefore, the probe antenna is suitable for linear measurement of the AUT in the angle range from –45° to 45°.

It is also worth mentioning that due to the back lobe of the probe antenna, reflections behind the antenna can have an effect on the measurement. To minimize these reflections, the antenna is mounted on a circular aluminum plate with a diameter of 400 mm which is additionally covered with pyramidal RAM. The probe antenna is extended by a waveguide to protrude 300 mm from the plate since the angle from the antenna to the edge of the absorber collar should be at least 120° [19]. Figure 4.9 shows the probe antenna mounted on the slider of the linear axis.

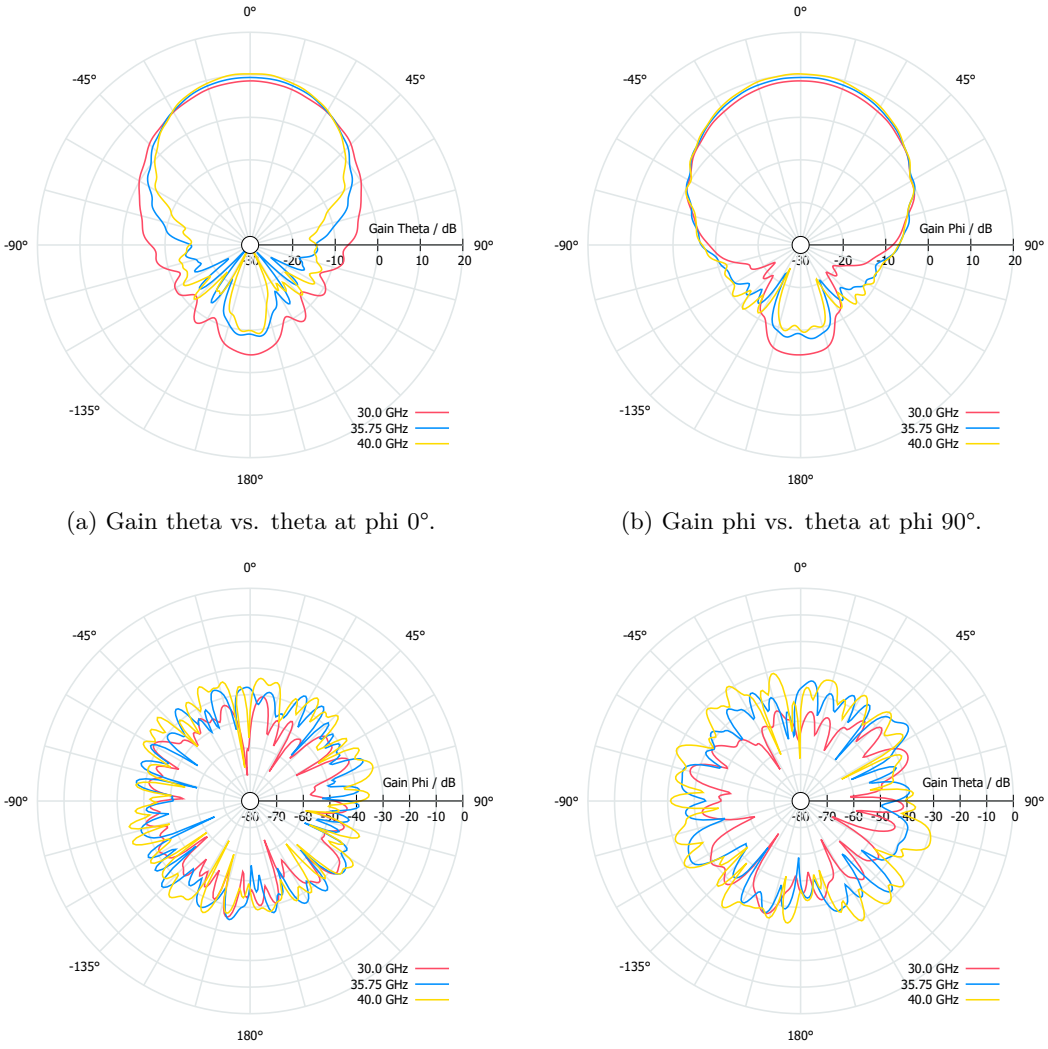

(a) Gain theta vs. theta at phi 0°.

(b) Gain phi vs. theta at phi 90°.

(c) Gain phi vs. theta at phi 0°.

(d) Gain theta vs. theta at phi 90°.

Figure 4.8: Probe horn antenna gain at co-polarization (a and b) and cross-polarization (c and d) simulated at phi 0° (a and c) and phi 90° (b and d).

4.1.6 Minimum Antenna Distance

There are different areas around an antenna in which the electromagnetic field is constituted differently, as described in Section 2.1.4. In order to measure the antenna characteristic, the probe antenna should be located in far field, where the characteristic is measured with correct reference to the angle between probe and AUT and furthermore the wave propagation of the AUT is not influenced. There are also methods to measure the antenna in near field (near field scanners), but these require an extensive knowledge of the probe antenna and the environment to mathematically correct the influence of the probe.

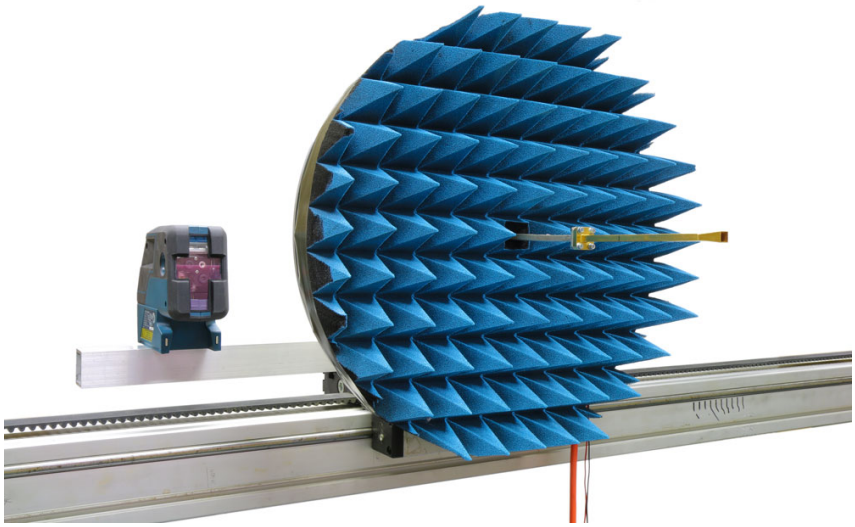

Figure 4.9: Extended probe antenna mounted on at the slider of the linear axis on a circular, 400 mm aluminum plate with absorber collar.

The minimum distance between both antennas is given by Equation 2.12. For this purpose the largest aperture size and the maximum measurement frequency of both antennas are used, which corresponds to a size of $D = 36.75$ mm of the slotted waveguide antenna and a frequency of $f = 40$ GHz. This results in a minimum antenna spacing of $R > 360$ mm. Considering the drive path of the linear axis and to reduce its required positioning accuracy (see next section), a distance of 700 mm between the probe antenna and AUT is selected.

4.1.7 Feed Antenna Positioning

A motorized linear axis is used to place the probe in relation to the slotted waveguide antenna. This axis is driven by a stepper motor and can be adjusted in its position with an accuracy of ± 1 mm. It provides a sufficient and reproducible positioning of the probe antenna. The motor is controlled via MATLAB using the Instrument Control Toolbox. Thereby, a script is designed in which the linear axis stops during the RF measurement and subsequently moves to the next position. The linear axis is aligned parallel to the front of the climatic chamber. A laser is attached to the slider to align center of the axis and AUT. It projects a line on the climatic chamber and two points orthogonal to this line in the direction of axis which allows the alignment of the laser on the axis.

The linear axis has a drive path of 1.8 m. The distance between test object and probe antenna is set to 700 mm which is inside the far-field and enables to cover

the AUT from theta –45° to 45°. Furthermore, the distance is large enough that with a positioning accuracy of ±1 mm only a maximum angular error of ±0.081° occurs. Due to the linear track of the axis, the distance to the AUT changes and the positions on the axis are not equidistant by attaining equal angular steps. By using the tangent function in MATLAB the linear axis is controlled in such a way that the angular steps are of the same size.

4.1.8 Mounting of the Antenna Under Test

In order to place the AUT in the temperature chamber, a mounting is designed which also allows the antenna to be tilted in elevation. A temperature sensor is attached to the mounting, which enables the exact determination of the antenna temperature, while the antenna mounting is attached to the ground plate of the temperature chamber to ensure stable positioning. Figure 4.10 shows the antenna mounting.

Using the distance of AUT and probe antenna, an error estimation due to internal thermal expansion within the temperature chamber is performed. Both, the inside of the climatic chamber and the antenna mounting are made of aluminum. The inside width of the temperature chamber is 650 mm. At a temperature difference of 90 K and a CTE of $23.8 \cdot 10^{-6}$ K^{-1} [20] a total length change of approximately 1.4 mm will occur. Even in the unlikely event that the antenna experiences the entire change in length in one direction, this only results in an angular error of 0.12° at a distance to the probe antenna of 700 mm.

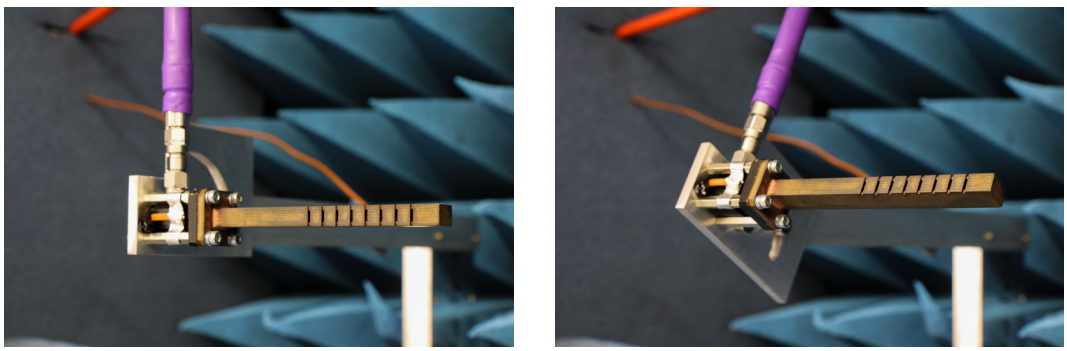

(a) (b)

Figure 4.10: Mounting of the AUT within the temperature chamber at 0° elevation (a) and 20° elevation (b).

4.1.9 Measuring Instruments

The acquisition of the antenna characteristic is performed using a network analyzer which determines the scattering parameters between port 1 to which the AUT is connected, and port 2, which is connected to the probe antenna. The forward transformation coefficient S_{21} is used to determine the characteristics of the AUT. Also, the input reflection coefficient S_{11} of the AUT at different temperatures is measured.

During measurement, high requirements are placed on the RF signal chain with regard to dynamics. For instance, the network analyzer has to detect very weak signals of the slotted waveguide antenna during measurement in cross-polarization. Therefore, a low noise amplifier (LNA) with a gain of 36 dB (typical) and a noise figure of 2.8 dB (typical) is connected directly after the probe antenna in order to minimize an increase of the noise floor and amplify the received signal.

The settings of the network analyzer also have a significant influence on the performance of the measurement setup. The most important settings of the device are listed below.

Frequency Range The frequency range is set from 30 GHz to 40 GHz, leaving open the possibility to detect changes in the antenna characteristics over a wide frequency range.

Source Power The source power is set to the highest possible value of –3 dBm in order to generate maximum field strength at the probe antenna.

Number of Points The number of sampling points determines how well the measurement is resolved. This value is not only important for displaying the results, but also for the time domain of the signal when performing an inverse Fourier transformation. A high number of measurement points also increases the measurement time of one frequency sweep. A value of 601 sample points is used in this practical examination.

IF Bandwidth On the one hand, the resolution bandwidth determines the measurement dynamics of the internal receiver of the network analyzer significantly,a small resolution bandwidth also leads to a long measurement time. A resolution bandwidth of 10 kHz is used as a compromise, thus, the level of forward transmission coefficient in cross-polarization is approximately 20 dB above the noise floor and the measurement time is about 1 second per sweep.

The settings of the network analyzer are saved as a setup file in the internal memory of the instrument where it is restored during initialization of the measurement.

The network analyzer is controlled by MATLAB via VISA interface. It is connected to the computer via USB and can be controlled using SCPI commands. Before starting the measurement, the instrument is presetted with the setup file described above. A frequency sweep is performed for each angular step and the data is transferred directly to the computer via VISA interface. As to save the transmitted data in a file similar Touchstone S2P, the real and imaginary values of the transmitted data are converted into magnitude and phase. For each angular step a single CSV file including stimulus and all four of the two-port scattering parameters is saved on the computer during measurement. The responsible code excerpt is shown in Section B.1.

The motor controller is connected to the computer via a serial interface and can also be controlled via MATLAB. The slider is positioned to equal angular steps to the antenna. While performing the measurement with the network analyzer the axis remains in its position. The slider is positioned in 0.2° steps in range from –45° to 45°, resulting in 451 points to be approached in order to resolve the antenna diagram with sufficient accuracy. The total measurement time for an antenna segment is approximately 20 min.

4.1.10 Final Measurement Setup

Figure 4.11 shows the final measurement setup in a schematic representation. The actual implementation of the measurement setup is shown in Figure 4.12, while the used components are listed in the appendix under Chapter A in detail.

4.2 Measurement Procedure

The main objective of the measurement is to characterize the AUT in co- and cross-polarization at different temperatures. On the one hand, the expected temperature range for airborne SAR systems is defined in Section 1.2.2 from 30 °C to –55 °C, the temperature chamber, on the other hand, only allows temperature conditioning down to –40 °C. In order to maintain the difference in temperature, the upper temperature limit is raised from 30 °C to 45 °C.

To recognize trends in the antenna characteristic due to temperature changes, the measurement is performed at the temperature limits as well as at two further sampling points. To keep the difference in temperature between the sampling points equal, the upper temperature limit is lifted from 45 °C to 50 °C. Thus, by selecting

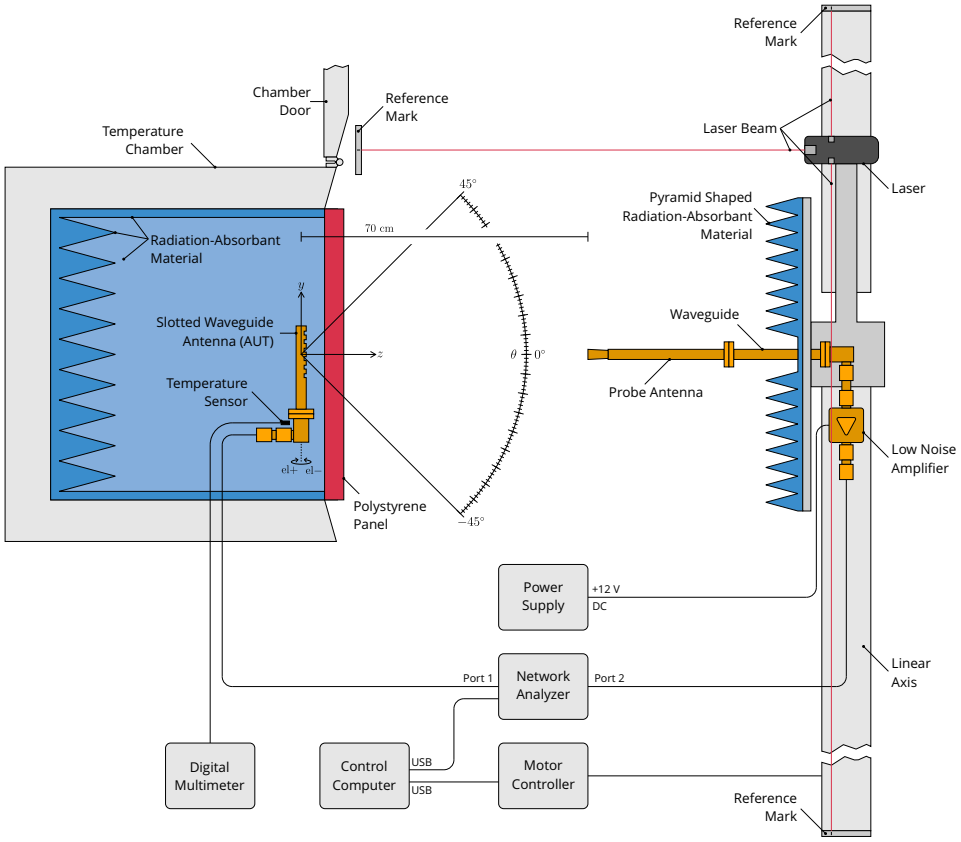

Figure 4.11: Schematic representation of the measurement setup (non proportional).

the antenna temperatures of 50 °C, 20 °C, 10 °C and 40 °C, an equal temperature difference of 30 K is achieved.

At any temperature, both, the plastic-printed antenna and the brass antenna are measured in co- and cross-polarization. The measurements of the antennas in DLR's compact test range (CTR) have shown that at 0° elevation very low cross-polarization component is received. Therefore, the measurement in vertical polarization is performed at 20° elevation. For co-polarization, on the other hand, the highest signal amplitude is expected at 0° elevation. This is visible in the CTR measurement as shown in Figure 4.13.

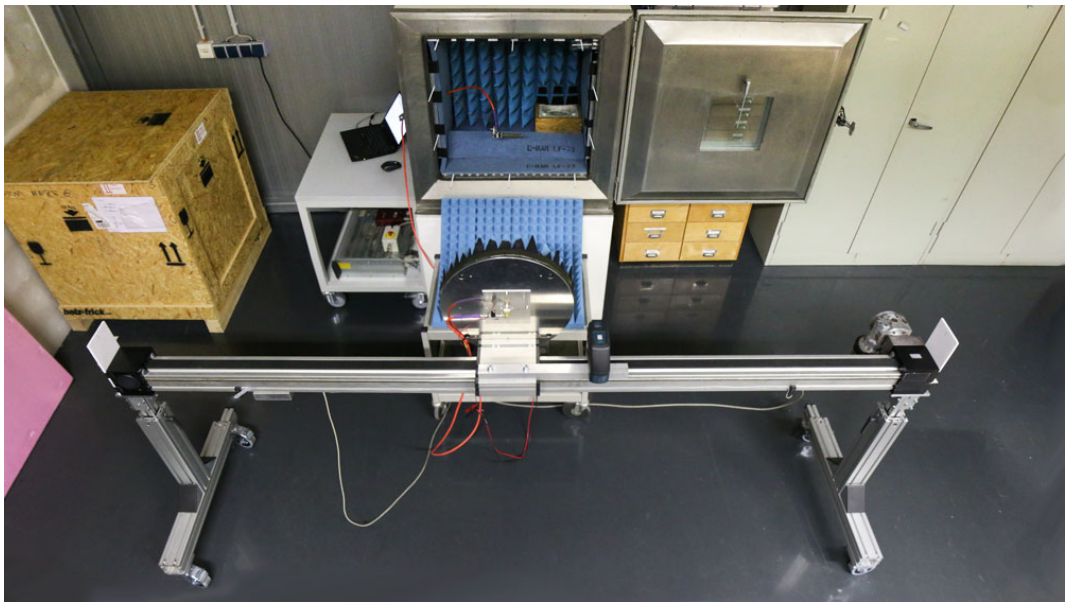

Figure 4.12: Photo of the measurement setup.

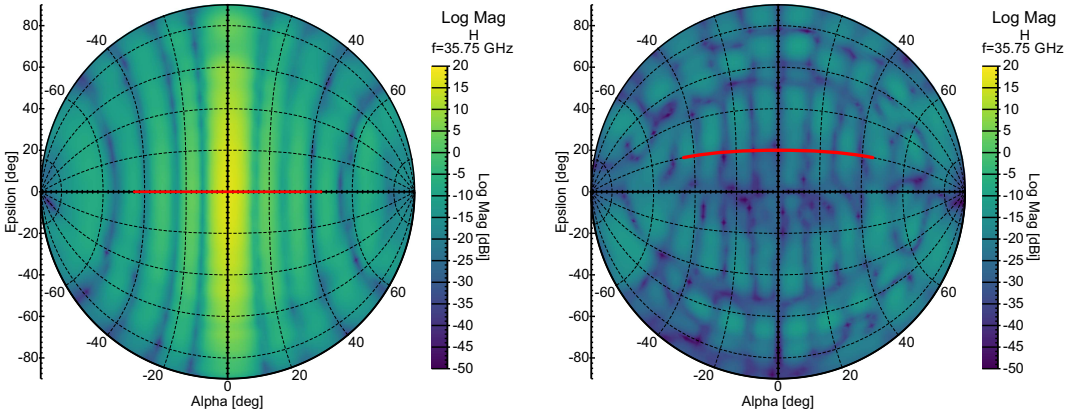

(a) (b)

Figure 4.13: Measurement results of the plastic printed antenna in DLR's compact test range in co-polarization (a) and cross-polarization (b). The red line indicates the cross section to be measured in this thesis.

4.3 Raw Measurement Data

In the following, the unprocessed measurement results are presented. The input reflection coefficient, the forward transmission coefficient in horizontal polarization and the forward transmission coefficient in vertical polarization are examined for the brass and the plastic antenna.

4.3.1 Input Reflection

Figure 4.14 and 4.15 show the input reflection coefficient of the antennas at different temperatures. The comparison of the data is difficult, as the input reflection of the antenna seems to be superimposed by an interfering signal causing a ripple on the measured reflection coefficient. The characteristics of this interfering signal are the same for each measurement series. Due to the uncalibrated measurement with the network analyzer, this measurement represents the input reflection of the entire signal chain. Accordingly, the displayed characteristics do not correspond to the input reflections of the antennas themselves. Therefore, these data sets are not suitable to characterize the temperature behavior of the antennas.

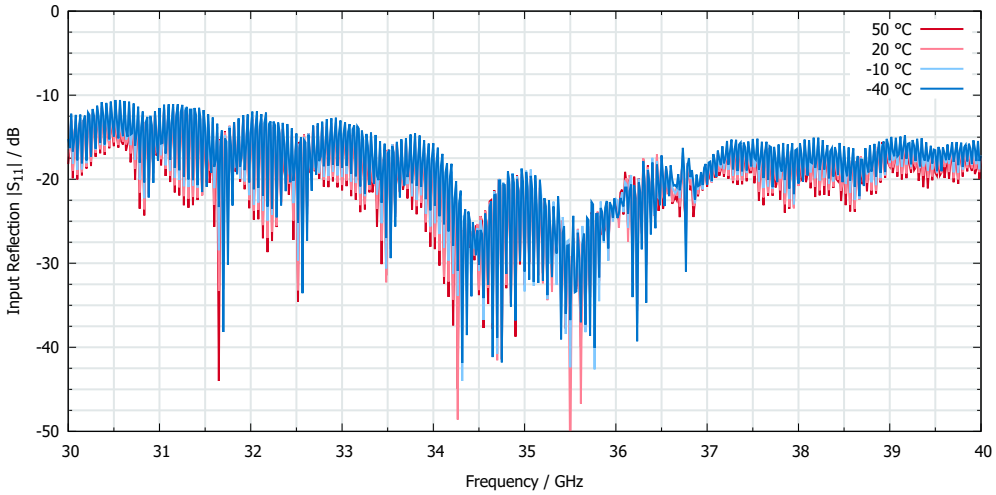

Figure 4.14: Raw measurement data of the input reflection coefficient of the brass slotted waveguide antenna at different temperatures.

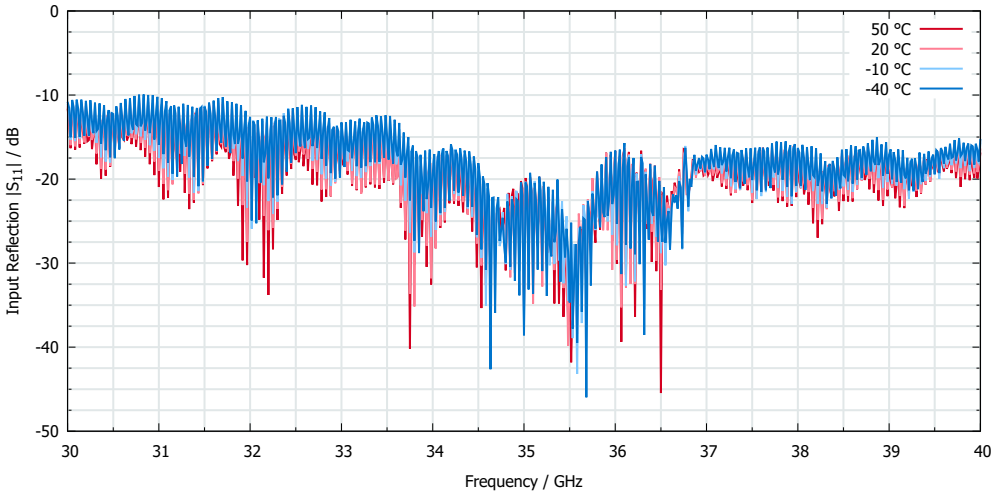

Figure 4.15: Raw measurement data of the input reflection coefficient of the plastic printed slotted waveguide antenna at different temperatures.

4.3.2 Forward Transmission (Antenna Pattern)

The measured values of the forward transmission coefficients are also superimposed by one or more interference signals. The data sets are not suitable to characterize the forward transmission of the antennas at different temperatures.

Co-Polarization

The measurement data in horizontal polarization at high theta angles are superimposed by interfering signals. Very slight shifts of the main lobe of the plastic antenna is recognizable despite the superimposing signal due to the high amplitude at the main lobe. The amplitude of the signal seems to change with temperature at both antennas, however, it must be examined whether this effect is attributable to the antenna.

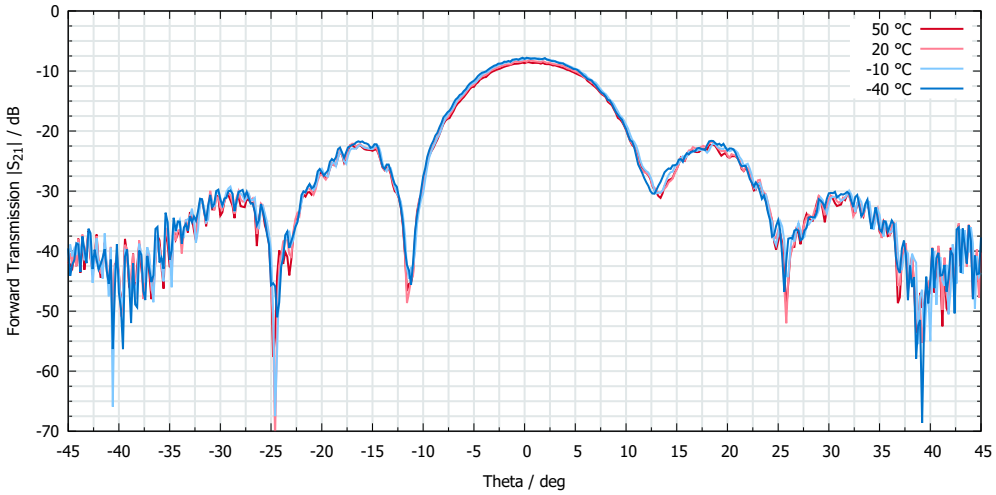

Figure 4.16: Raw measurement data of the forward transmission coefficient at 35.75 GHz in co-polarization of the brass antenna at a mounting angle of 0° elevation at different temperatures.

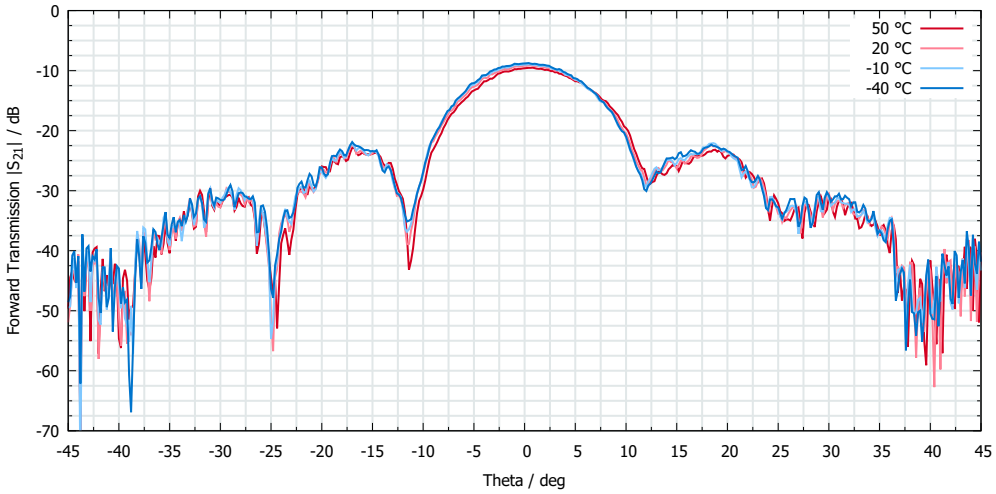

Figure 4.17: Raw measurement data of the forward transmission coefficient at 35.75 GHz in co-polarization of the plastic antenna at a mounting angle of 0° elevation at different temperatures.

Cross-Polarization

The measurement data in cross-polarization are difficult to differentiate due to the weak signal amplitude and the relatively strong superposition of interfering signals. It is not possible to draw a conclusion about the temperature behavior with the raw data.

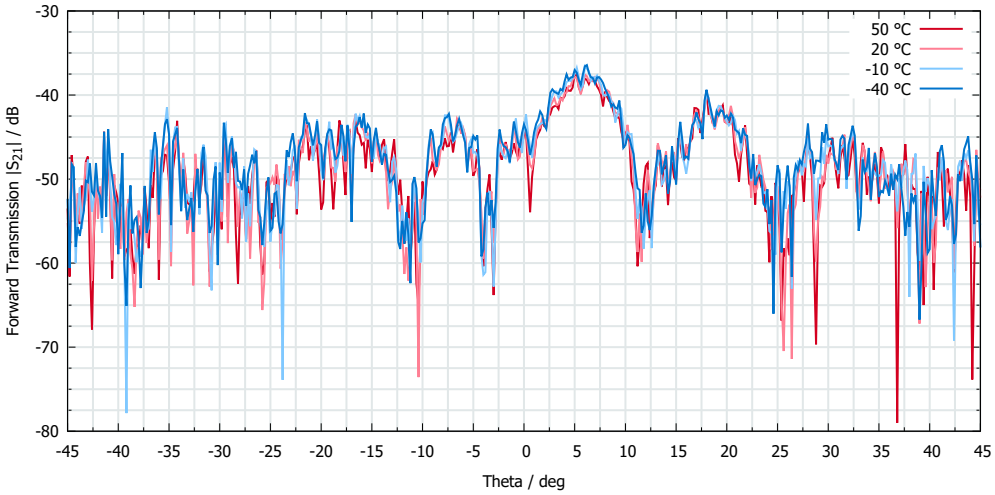

Figure 4.18: Raw measurement data of the forward transmission coefficient at 35.75 GHz in cross-polarization of the brass antenna at a mounting angle of 20° elevation at different temperatures.

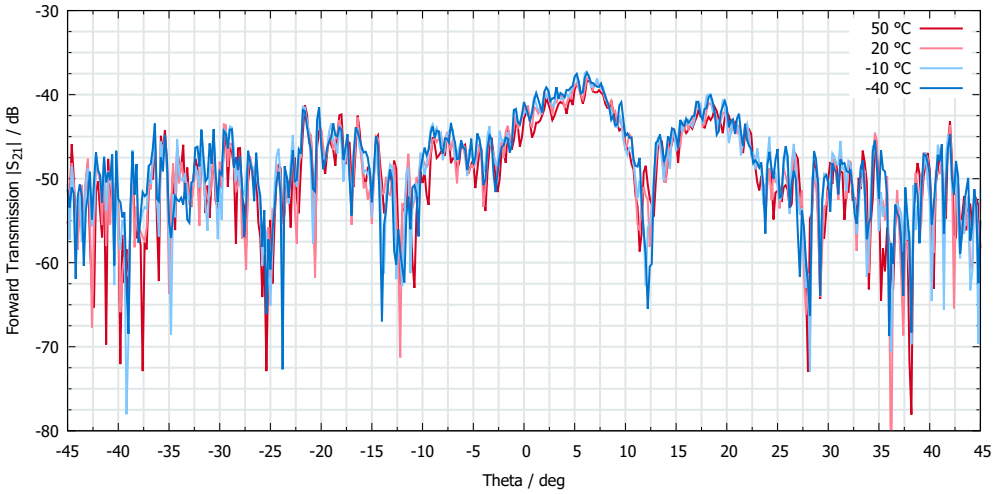

Figure 4.19: Raw measurement data of the forward transmission coefficient at 35.75 GHz in cross-polarization of the plastic antenna at a mounting angle of 20° elevation at different temperatures.

CHAPTER 5

POST-PROCESSING OF MEASUREMENT RESULTS

This chapter is about the improvement and subsequent analysis of the acquired data. The objective is to apply algorithms to improve the data quality without the need of further advancement of the measurement setup, as this would be time-consuming and cost-intensive.

The first section deals with the cable's temperature response to remove this effect from the measured data. In a further step, the signal is transformed into time domain in order to analyze the interfering signals in the raw data. After the suppression of the interfering signals in time domain, the data is transformed back into frequency domain. The chapter concludes with the final analysis of the processed data.

5.1 Temperature Behavior of RF Cables

The measurement results in Section 4.3 point out that the forward transmission coefficient of the measurement setup changes in amplitude over temperature. Since a part of the RF cable is also located within the temperature chamber, its temperature behavior is examined in this section.

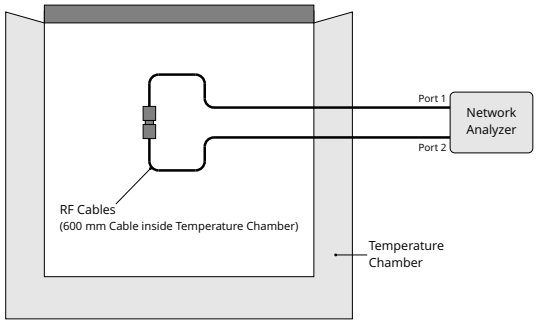

Figure 5.1: Measurement setup to determine the influence of temperature on the RF cables.

For this purpose, an additional series of measurements is carried out in which a second, identical cable is inserted into the temperature chamber and thus forms a loop, as Figure 5.1 illustrates. Thereby, the length of the cable inside the climatic chamber is twice as long as the length used to perform the antenna measurement.

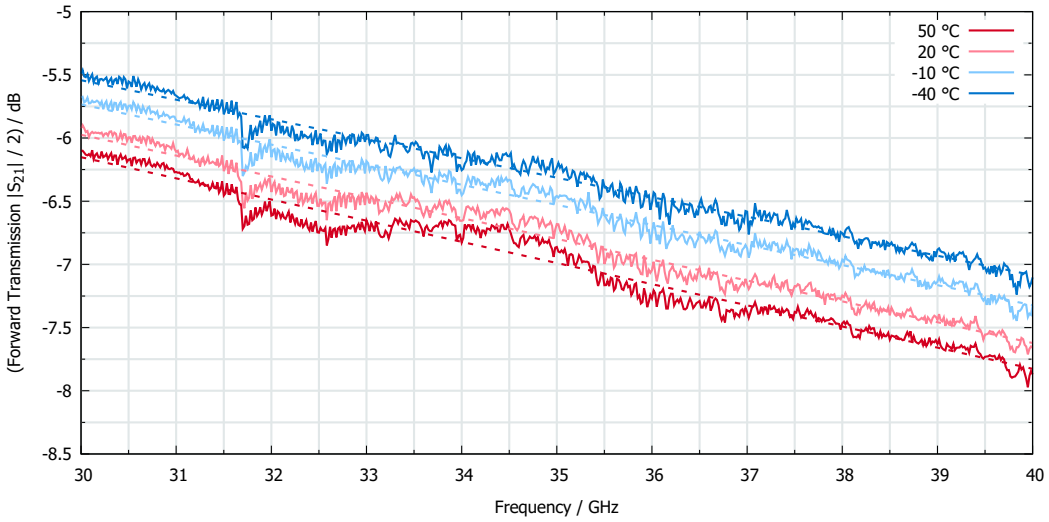

Figure 5.2: Half of the forward transmission coefficient ($|S_{21}|/2$) of the cable loop over temperature (solid) and the corresponding polyfitted data (dashed).

A first look at the measurement results shows that the cables exhibit very similar temperature behavior, as the insertion loss also increases with rising temperature. A linear approximation of the data is performed to calibrate the antenna measurement by using MATLAB. For this purpose the MATLAB function `polyfit()` is used. Figure 5.2 illustrates the measurement data as well as the polyfitted data.

5.2 Multipath Propagation

The measurements performed in Section 4.3 show a strong superposition with interfering signals. Noise is excluded as cause for this disturbance, as the noise floor is significantly reduced by shielding the probe antenna and the disturbing signal has a repeatable pattern throughout the measured angle range. The reproducibility of the interference in relation to the angle indicates a problem related with the geometrical shape of the surrounding environment.

By taking a look at the measurement setup, it becomes apparent that there are still many metallic surfaces in the immediate vicinity of the slotted waveguide antenna and probe antenna which cause reflection of the radiated signal. Furthermore, it is possible that the radiated horizontally polarized signal will reflect on surfaces

and change its polarization angle. Thus, while measuring the weak signal in vertical polarization, the reflections may interfere with the measurement. Particularly at the front of the temperature chamber, reflections can occur unhindered. A further lining of the surfaces with RAM is almost impossible in the area of the polystyrene cover and would be very cost-intensive anyway. Consequently, another possibility to reduce the influence of multipath propagation on the measured data has to be figured out.

During measurement of the antenna only the signal propagating directly from the AUT to the probe is the one that has to be detected. Other parts of the signal which are first reflected on a surface and then captured by the probe antenna do not belong to the directly received signal from the antenna and can therefore be ignored in the measurement. The signals received directly and those, received due to reflection, differ in time of arriving of the signal at the probe antenna. Whereas the direct signal always takes the least amount of time from AUT to probe antenna, a reflected signal arrives later due to the longer distance. This property is used to confine the data to directly received signals only.

5.2.1 Signal Propagation Time

In the following, the propagation time within the signal chain is determined theoretically. The propagation time of a signal results from the distance traveled and the speed at which the wave propagates. The speed of propagation of the electromagnetic wave in air can be equated without great error with its velocity in vacuum, and is, therefore, the speed of light. In other media, such as the coaxial lines or waveguides used in this application, the electromagnetic wave propagates at a lower velocity. The ratio of actual velocity in medium to the speed of light is called the velocity factor (VF).

For the coaxial cables in use this velocity factor is taken from the manufacturer's data sheet and in this case 69% of the speed of light. For sake of simplicity, this value is assumed for all coaxial components.

The velocity factor of the waveguide components can be determined by their geometric dimensions. In general, the group velocity in the waveguide results from [6]:

$$v_\mathrm{g} = c_0 \sqrt{1 - \left(\frac{\lambda}{\lambda_\mathrm{c}}\right)^2} \quad . \tag{5.1}$$

Thereby, the free space wavelength λ is the quotient of the speed of light c_0 and the frequency f. The cut-off wavelength of a rectangular waveguide is defined by the dimensions of the cross-sectional area a and b of the waveguide [6]:

$$\lambda_c = \frac{2\pi}{\sqrt{\left(\frac{m\pi}{a}\right)^2 + \left(\frac{m\pi}{a}\right)^2}} \quad . \tag{5.2}$$

This expression is simplified to $\lambda_c = 2a$ by taking only the TE_{10} mode into account. The group velocity of a rectangular waveguide is:

$$v_g = c_0 \sqrt{1 - \left(\frac{c_0}{2a \cdot f}\right)^2} \quad . \tag{5.3}$$

The velocity factor for a Ka-band waveguide at 35.75 GHz is, therefore, 80.76% of the speed of light. Table 5.1 shows an estimation of the signal propagation time in the used components.

The LNA is assumed with the velocity factor of the coaxial components since the coaxial connectors are very large in relation to its dimensions.

Table 5.1: Estimation of propagation time within the signal chain.

Component	Length / mm	VF / %	Time / ns
Network Analyzer	50	69.00	0.24
Coax Cable	2000	69.00	9.67
Adapter	10	69.00	0.05
Transition Coax to Waveguide	15	69.00	0.07
	15	80.76	0.06
AUT	87	80.76	0.36
Free Range	700	100.00	2.33
Probe Antenna	150.5	80.76	0.62
Waveguide	177.8	80.76	0.73
Transition Coax to Waveguide	15	80.76	0.06
	15	69.00	0.07
Adapter	10	69.00	0.05
LNA	25	69.00	0.12
Adapter	10	69.00	0.05
Coax Cable	2000	69.00	9.67
Network Analyzer	50	69.00	0.24
Sum	**5330.3**		**24.41**

5.2.2 Transformation into Time Domain

The transformation of the discrete frequency spectrum into time domain is done by the inverse discrete Fourier transformation using the fast Fourier transform algorithm that is implemented in the MATLAB `ifft()` function. The length of the time domain results from the quotient of the number of points to the bandwidth in the frequency domain. The code for calculating the inverse Fourier transformation of a S2P data structure can be found in Section B.2.

In order to get an exact time signal by a Fourier transformation, an infinite frequency spectrum is required. Since the measured spectrum is always limited, the time signal is subject to an error which can be derived by the transformation of the rectangular window which limits the frequency spectrum. The limitation can mathematically be described as a multiplication of the spectrum with a rectangular function, which corresponds to the convolution of the actual time signal with a sinc function. This leads to widening of sharp impulses in time domain, as can be explained by the convolution of the sinc function with a Dirac impulse. The width of the sinc impulse can be calculated by Equation 5.4. As a consequence, the transformation of a time-limited spectrum makes it more difficult to separate individual impulses from each other [21].

$$\Delta T = \frac{2}{\Delta F} \tag{5.4}$$

Figure 5.3 shows the into time domain transformed spectrum of the co- and cross-polarized measurement data of the plastic printed antenna. At 24.5 ns a clear peak is visible and corresponds to the total propagation time calculated in Table 5.1 which represents the directly transmitted signal. Prior to this peak only noise can be measured, whereas after the peak additional signals can be detected, which are caused by reflections.

The frequency spectrum of the input reflection coefficient can also be transformed into time domain as shown in Figure 5.4. The highest occurring peak marks the first reflection of the wave at the antenna. The signal occurs after a time of 21 ns which is twice the signal propagation time from the network analyzer to the antenna. Shortly before that point, at 19.8 ns, the reflection of the 2.4 mm to 2.92 mm adapter is visible. The peak at 42 ns corresponds to the repeated reflection of the signal between antenna and network analyzer.

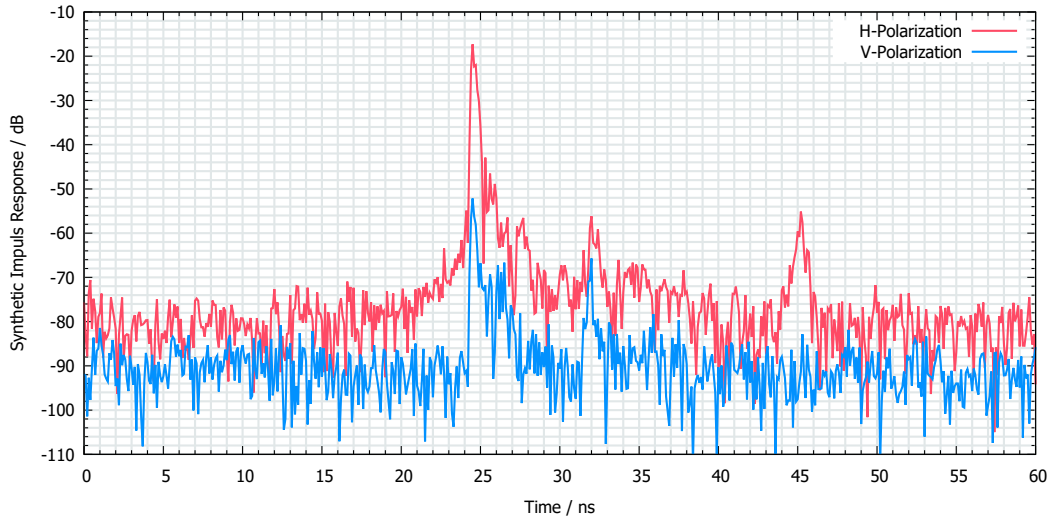

Figure 5.3: Synthetic impulse response of the measurement setup in horizontal and vertical polarization using the plastic printed AUT at 20 °C.

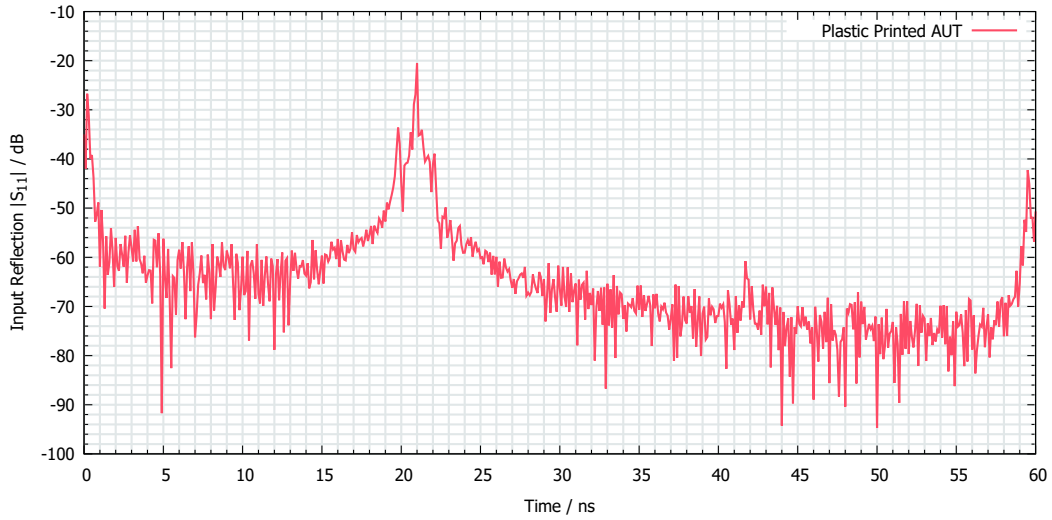

Figure 5.4: Input reflection coefficient of the plastic printed AUT in time domain at 20 °C.

An alternative way of representing the signal in time domain is a waterfall plot. The amplitude of the signal is color coded and displayed in a two-dimensional diagram. The abscissa represents the time axis, the ordinate the angle theta to the object. Figures 5.5 and 5.6 show this type of representation based on the example of the plastic printed antenna in horizontal and vertical polarization.

In the example of the horizontal polarization in Figure 5.5, the increase in distance between AUT and probe antenna towards high incident angles can be seen in form of a crescent on the waterfall plot. All signals arriving after this line are due to

multipath propagation. These undesired signals, which can be clearly differentiated in time domain, represent the undesired superposition in frequency domain.

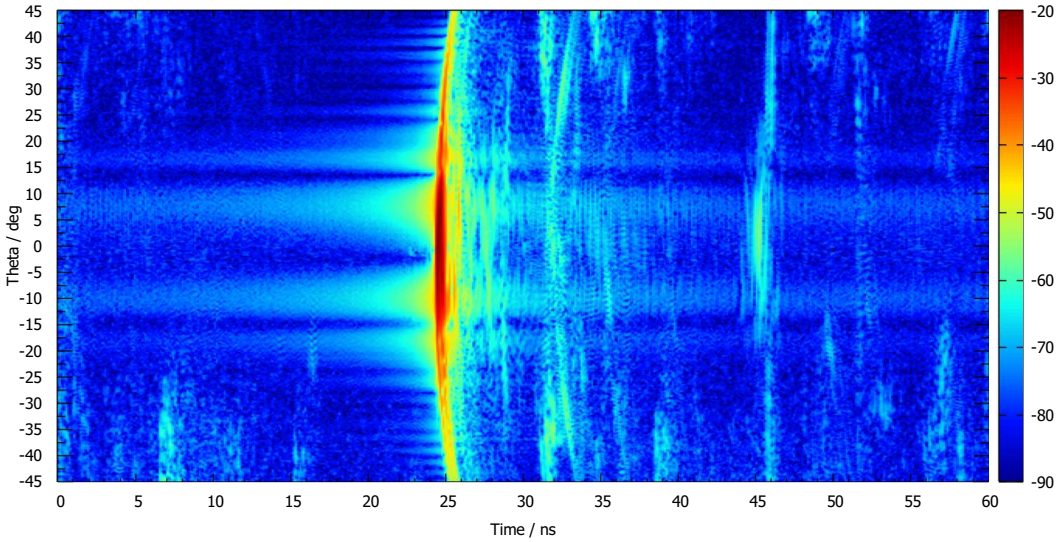

Figure 5.5: Waterfall plot of the synthetic impulse response of the measurement setup in horizontal polarization using the plastic printed AUT at 20 °C.

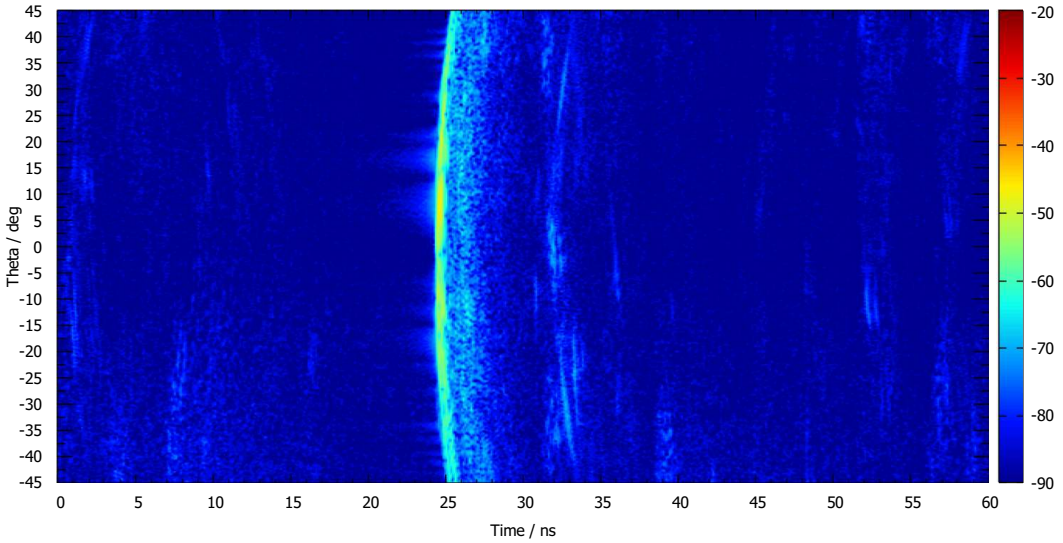

Figure 5.6: Waterfall plot of the synthetic impulse response of the measurement setup in vertical polarization using the plastic printed AUT at 20 °C.

5.3 Time Gating

The previous analysis of the signal in time domain shows that in addition to the directly propagating wave many further signals are received at a later time. While those interfering signals are almost impossible to differentiate in the frequency spectrum, they are easy to separate in time domain.

In order to reduce undesired signals in the frequency spectrum, it is advisable to suppress them in time domain. A very simple method is used, where signals outside a so-called time gate are replaced by noise. The time gate must contain all directly received signals, otherwise the characteristics of the antenna will not be displayed correctly during the reverse transformation of the signal. The widening of the signals during the Fourier transformation of the limited spectrum must be taken into account by choosing the width of the time gate. The additional width can be determined from the width of the sinc function caused by the transformation of the window of the frequency spectrum (Equation 5.4). For the measurement bandwidth of 10 GHz, the width of the gate must be increased by at least 200 ps. Furthermore, the convolution of the time signal with the sinc function due to the transformation of the limited spectrum may cause signals, which actually occurred before or after the time gate, but now reach into the time gate due to the infinite width of the sinc function. Thus, the direct received signal cannot be separated exactly.

Figure 5.7 shows the time gating of the input reflection coefficient of the antenna, which is performed with a simple rectangular window. All signals outside this window are exchanged by noise since a constant signal would generate a Dirac pulse during Fourier transformation. The noise is generated by MATLAB using the `randn()` function. The center of the time gate is 21 ns with a width of 1.2 ns.

In the case of the forward transformation coefficient, this window must be moved in accordance to the arrival time of the signal since the distance between AUT and probe antenna changes. At an angle of $\theta = 0$ the center of the gate is at 24.8 ns with a width of 1.2 ns. Figure 5.8 shows the time-gated signal of the forward transmission coefficients in vertical and horizontal polarization. At higher incident angles the time gate starts later according to the additional signal propagation time, as visualized in Figure 5.9. The entire gating algorithm is implemented in MATLAB and shown in Section B.3.

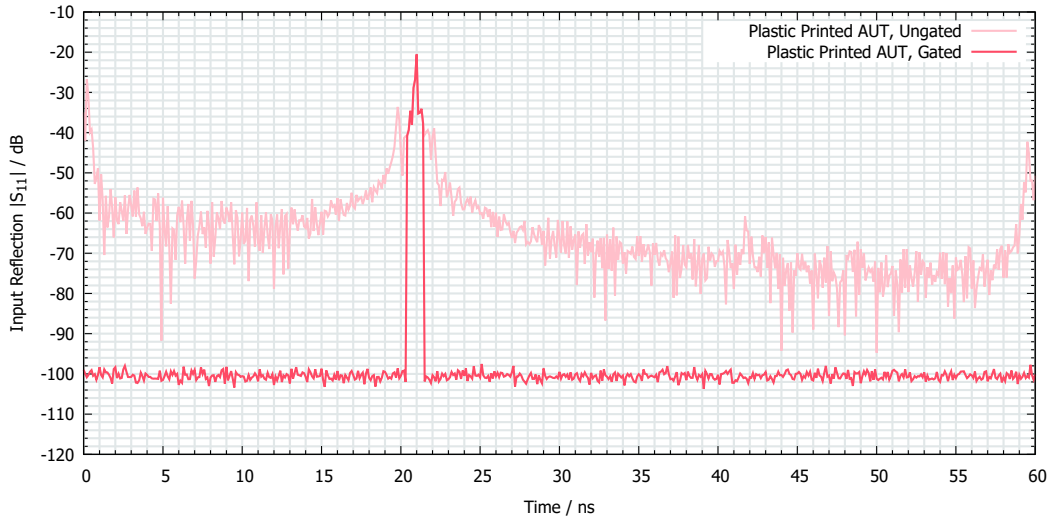

Figure 5.7: Time gated and ungated input reflection coefficient of the plastic printed AUT in time domain at 20 °C.

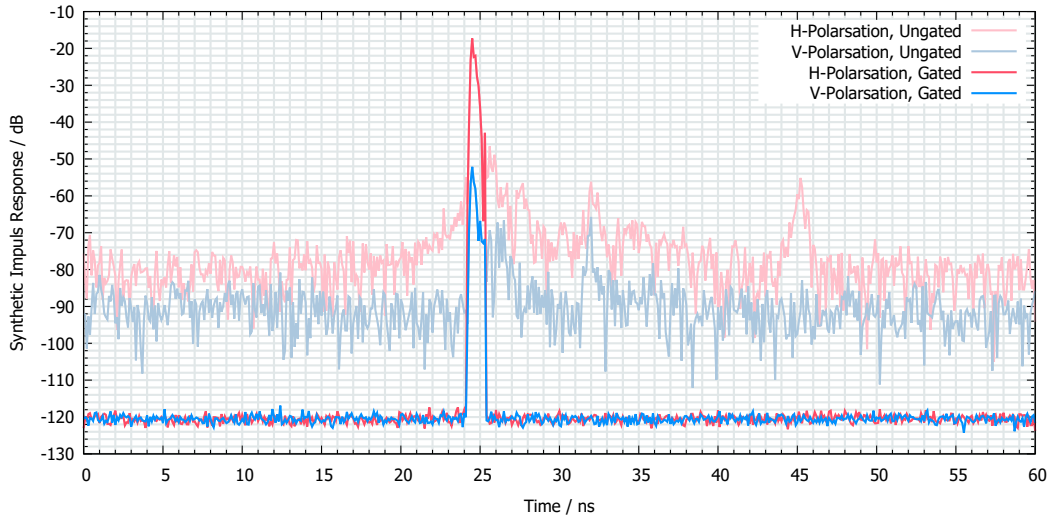

Figure 5.8: Time gated and ungated synthetic impulse response of the measurement setup in vertical and horizontal polarization using the plastic printed AUT at 20 °C.

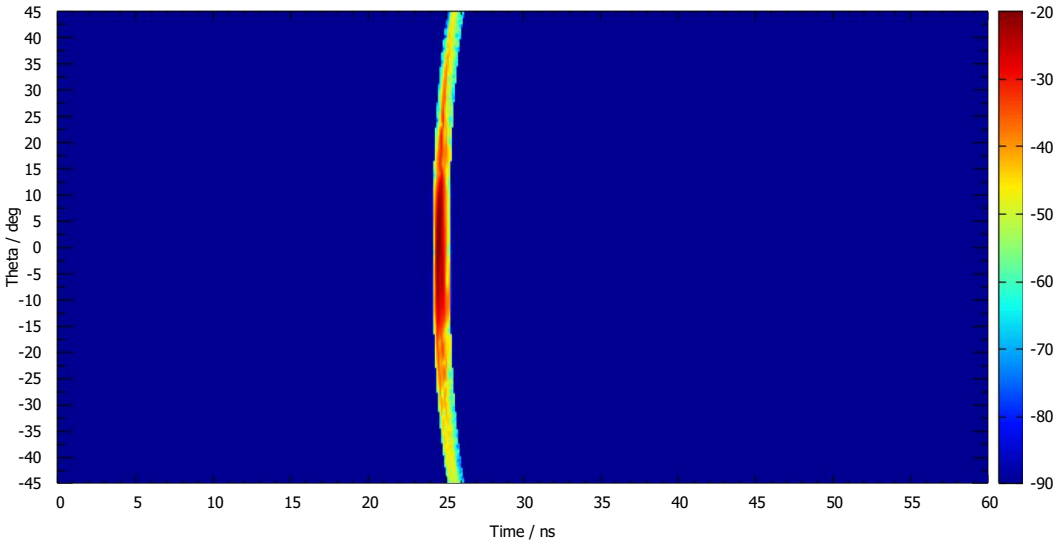

Figure 5.9: Waterfall plot of the time gated synthetic impulse response of the measurement setup in horizontal polarization using the plastic printed AUT at 20 °C.

5.4 Gating Results

To benefit from the time gating process the signal must be transformed from time domain back into frequency domain by using discrete Fourier transformation. This is performed by MATLAB using the fast Fourier algorithm implemented in the `fft()` function. The transformation back into the S2P similar data structure is performed in same manner as shown in Section B.1.

In the following, the results of the time gating are presented. Figure 5.10 shows the input reflection coefficient of the plastic printed slotted waveguide antenna before and after the usage of time gate. It turns out that the high frequency interference of the signal disappeared completely due to usage of time gating and the process of input reflection coefficient is clearly visible.

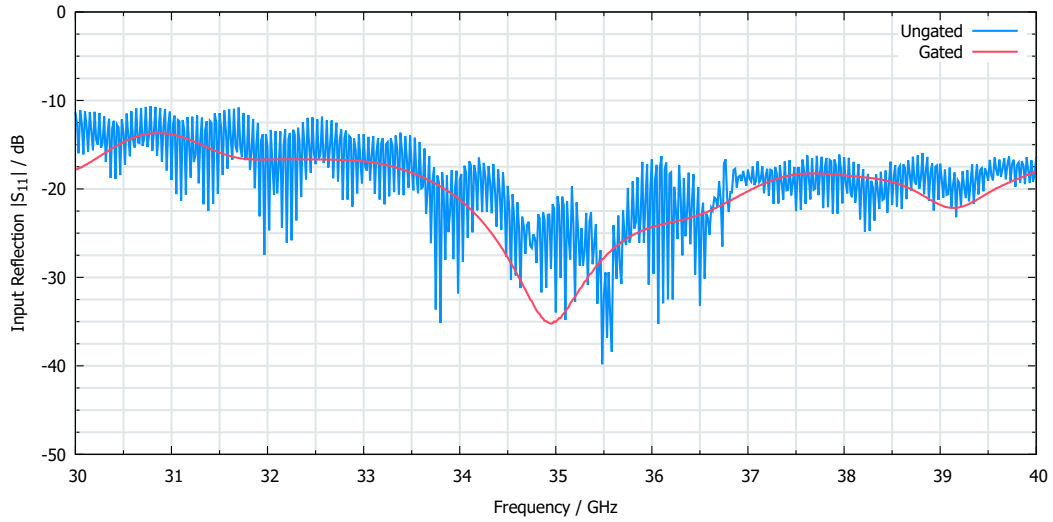

Figure 5.10: Comparison of the ungated and gated input reflection coefficient of the plastic printed AUT at 20 °C.

In case of forward transformation, identifying the signal after time gating is much easier as well and the measured data in horizontal polarization is improved to the high incident angles in particular.

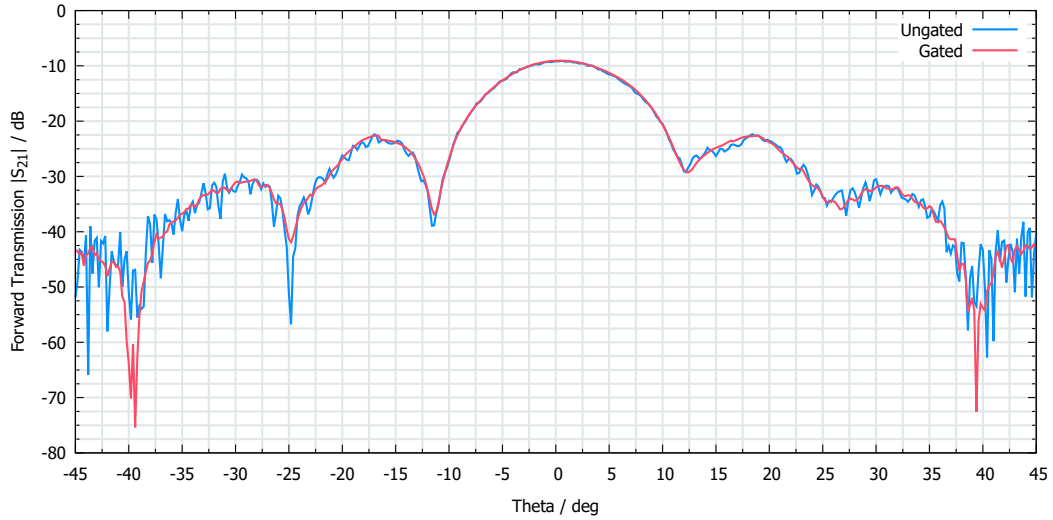

Figure 5.11: Comparison of the ungated and gated forward transmission coefficient of the co-polarized plastic printed AUT at 35.75 GHz, 20 °C, $\phi = 90°$ and 0° elevation in the azimuth range from –45° to 45°.

The measured data in vertical polarization show a significant improvement allowing an estimation of the amplitude behavior and the position of the zeros. In

summary, it can be said that time gating leads to an enormous qualitative improvement of the measurement data.

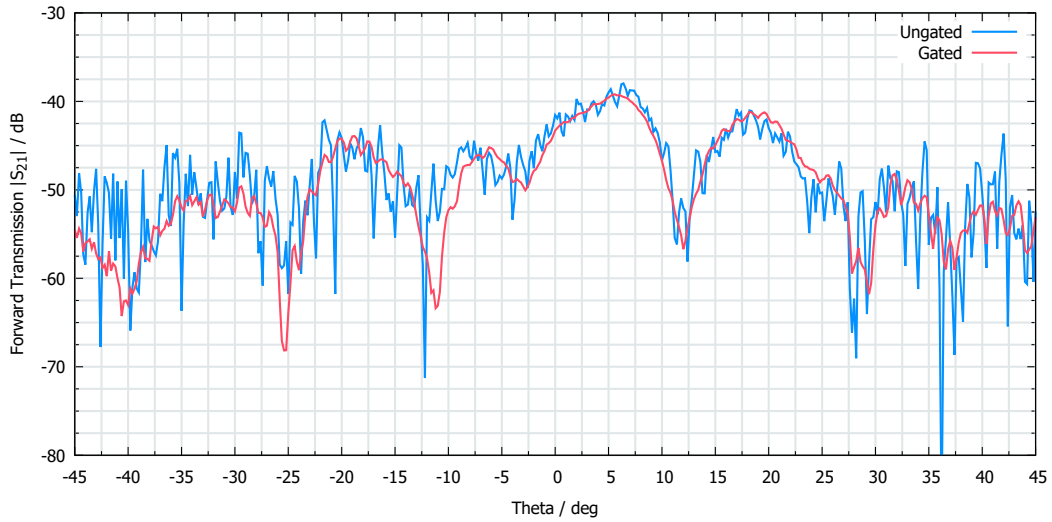

Figure 5.12: Comparison of the ungated and gated forward transmission coefficient of the cross-polarized plastic printed AUT at 35.75 GHz, 20 °C, $\phi = 90°$ and 20° elevation in the azimuth range from –45° to 45°.

The remaining ripple of the signal cannot be further suppressed since a finer selection of the time gate would have to be implemented which increases the risk of affecting parts of the actual signal. Remaining reflections probably occur within the signal chain.

5.5 Final Measurement Results

In this section, the final measurement results, based on the raw data in Section 4.3, are presented. They are corrected with the linear approximation of the cable's frequency response at different temperatures determined in Section 5.1. At this point it has to be mentioned that a correction of the temperature behavior is performed, but the frequency response is still not represented correctly since only one cable is calibrated. As the frequency response of the antenna is not relevant in this investigation, this type of correction is sufficient. In addition to the correction of temperature behavior of the cable, the antenna characteristic is filtered by the time gating method presented in the Section 5.3.

5.5.1 Input Reflection

Time gating of the data allows evaluation of the antennas' input reflection. The brass antenna shows a clear, but not very intense trend. When the antenna cools down from 50 °C to –40 °C, the position of the notch shifts by 100 MHz in direction of higher frequencies. In total, the input reflection coefficient increases by about 1 dB when the antenna cools down. The behavior of the measurement data thus corresponds very well with the simulation.

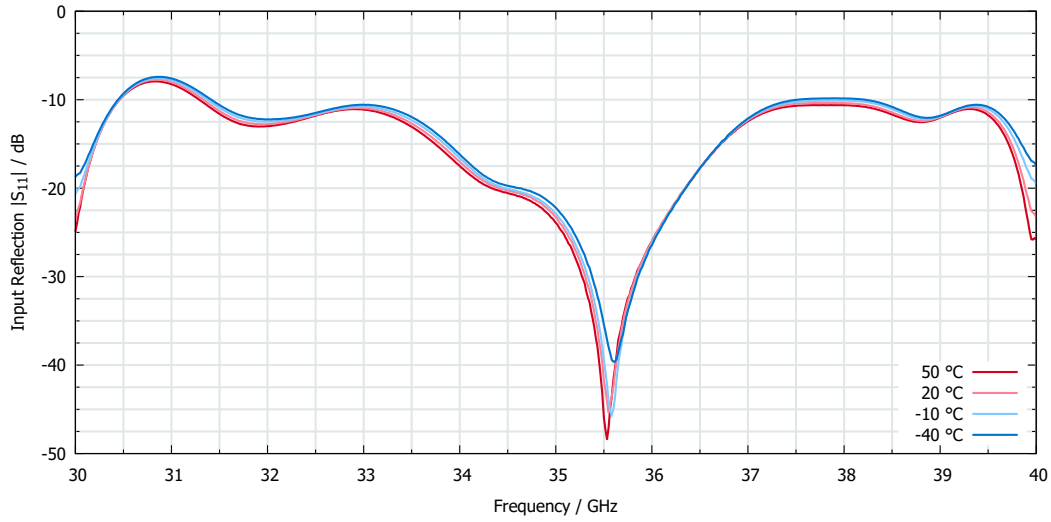

Figure 5.13: Input reflection S_{11} of the brass slotted waveguide antenna at different temperatures.

In case of the plastic printed antenna the simulation cannot be confirmed. In general, the input reflection increases by about 1 dB. The behavior of the notch, however, is different. The characteristic is less strong at high temperatures and the position of the notch remains almost at the same position.

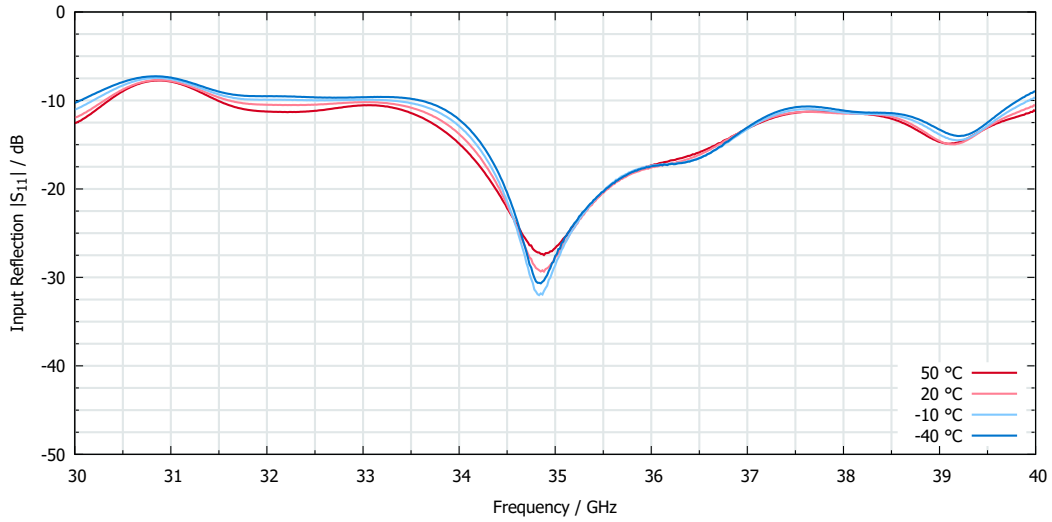

Figure 5.14: Input reflection S_{11} of the plastic printed slotted waveguide antenna at different temperatures.

With regard to input reflection, it can be stated that both antennas experience very little change over temperature. Whereas the brass antenna shows clear progress over temperature and confirms the simulation data, the plastic printed antenna experiences a much smaller change than expected.

5.5.2 Forward Transmission (Antenna Pattern)

Time gating also significantly improves the comparability of data of forward transmission coefficient. Especially in the vertical polarization, changes in antenna characteristics are now visible.

Co-Polarization

Figure 5.15 and 5.16 show the post-processed measurement results of the forward transmission in horizontal polarization. It is visible that the data sets fit together very well. Even for the larger angular ranges, which are difficult to measure due to lower amplitudes, the data are very similar for both, brass and plastic printed antenna. Removing the influence of the cable has also completely eliminated the variations in amplitude.

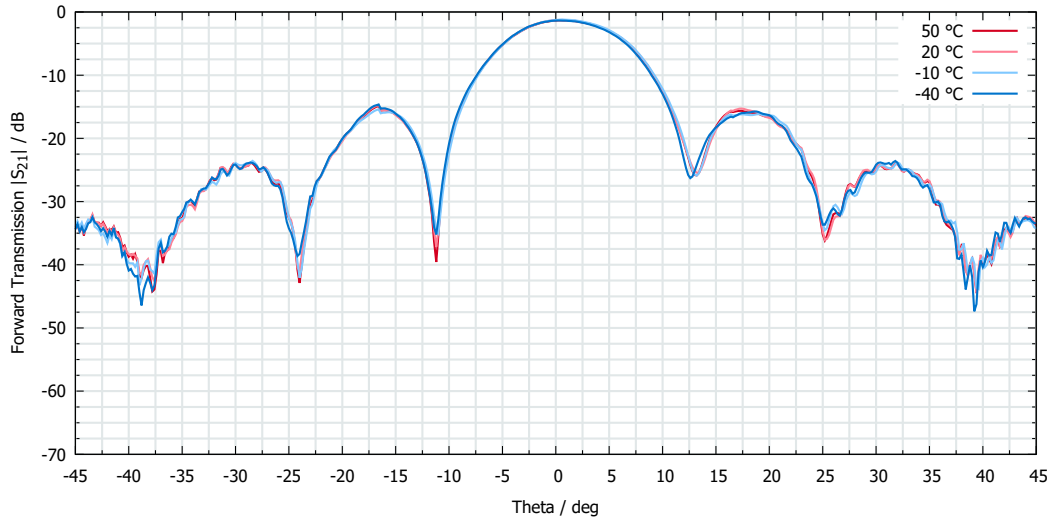

Figure 5.15: Forward transmission S_{21} at co-polarization of the brass slotted waveguide antenna at a mounting angle of 0° elevation at different temperatures.

As predicted in the simulation, the pointing of the plastic antenna deviates slightly towards positive theta angles at high temperatures. When determining the center of the 10 dB beamwidth, the brass antenna does not show a clear displacement, whereas the plastic antenna changes its pointing by approximately 0.8°.

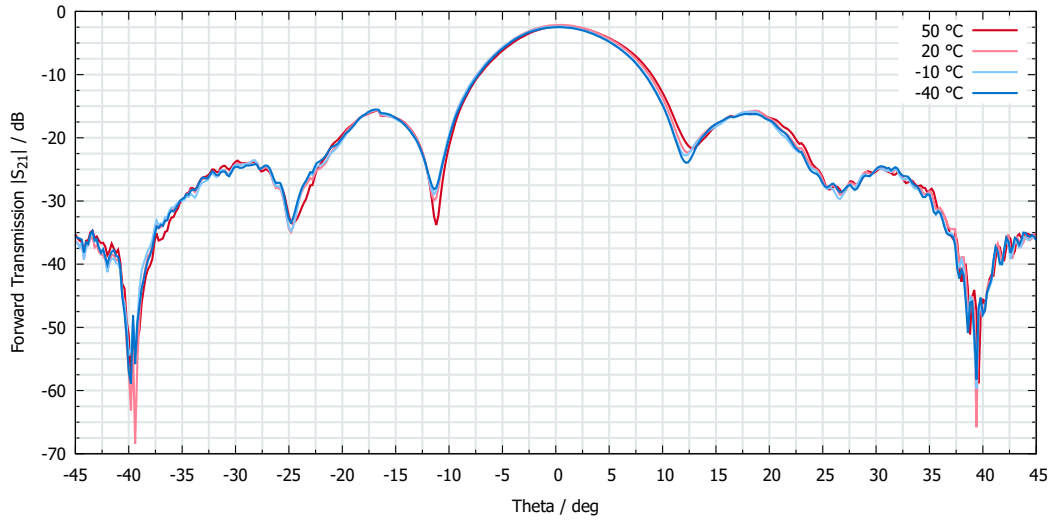

Figure 5.16: Forward transmission S_{21} at co-polarization of the plastic printed slotted waveguide antenna at a mounting angle of 0° elevation at different temperatures.

Cross-Polarization

Figure 5.17 and 5.18 show the post-processed measurement results of the forward transmission in vertical polarization. As well as in the simulation, the measurement of the antenna shows slight variations in forward transmission. However, the general course of transmission remains the same. The average deviation for the brass antenna is 0.5 dB whereas the average deviation for the plastic antenna is 0.7 dB which are excellent results.

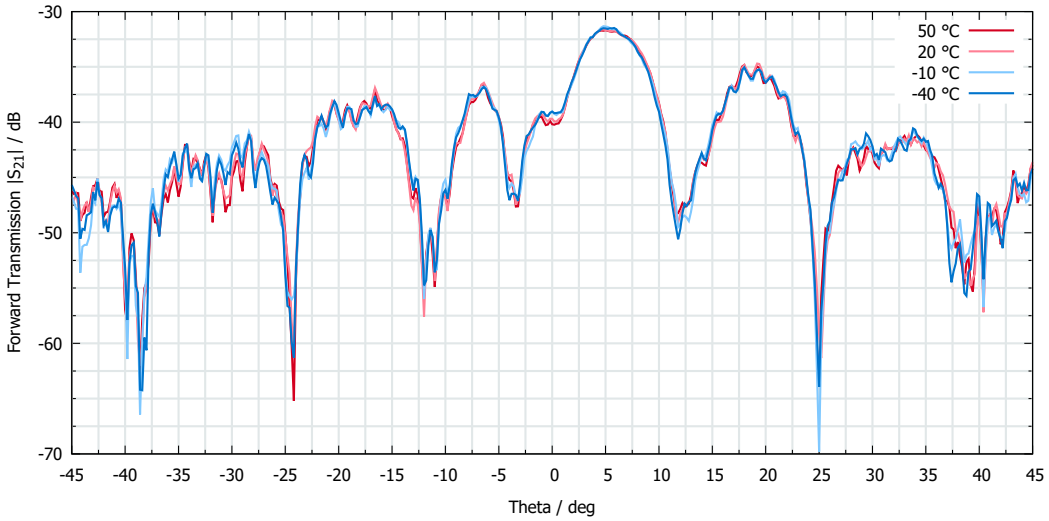

Figure 5.17: Forward transmission S_{21} at cross-polarization of the brass slotted waveguide antenna at a mounting angle of 20° elevation at different temperatures.

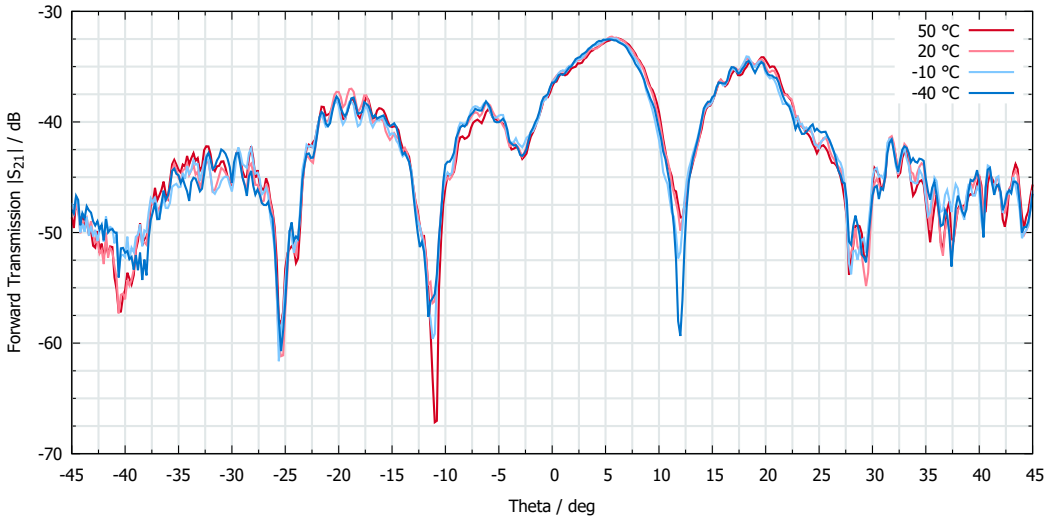

Figure 5.18: Forward transmission S_{21} at cross-polarization of the plastic printed slotted waveguide antenna at a mounting angle of 20° elevation at different temperatures.

CHAPTER 6

CONCLUSION

6.1 Conclusion

In this thesis, the behavior of two Ka-band slot antennas made of brass and plastic at different temperatures was investigated.

At the beginning of the analysis, a theoretical investigation of the antenna structure was carried out by simulation. At first, the thermal influences on the characteristics of the antenna were considered separately and then, the antenna was examined with their real parameters. It can be stated that thermal expansion has the greatest effect on the antenna characteristics. Simulated with realistic parameters, the antennas exhibit only very small differences in both antenna gain and input reflection.

To verify the simulation results, a measurement setup was developed to investigate the behavior of the antenna in dependence of temperature. The resulting measurement setup was realized with comparatively simple instruments and showed reproducible results. However, a high proportion of reflections superimposes the measurement signal which does not allow the evaluation of the data in last detail.

To improve the quality of the measurement data, a post-processing procedure was presented. The desired measurement signal was filtered in time domain by using time gating whereas the interfering signals were suppressed. This method led to a better interpretation of the measurement data.

The investigation of the antenna prototypes showed that within the for SAR applications expected temperature range from 30 °C to –55 °C no significant changes in the antenna characteristic occur.

The conclusion can be drawn that changes in temperature of the material mainly cause a change in the signal phase due thermal expansion and cross-sectional area of the waveguide [16]. The more elements are arranged within a resonant slotted waveguide array, the higher the error in phase assignment. On the one hand, com-

ponents with a fixed length, such as waveguides, experience a higher change in phase due thermal expansion at high frequencies. On the other hand, the phase change within components, such as slotted waveguide antennas, where the dimensions are in relation to the wavelength, remains the same at all frequencies, as long as the same ratio of wavelength to cut-off wavelength applies in the waveguide. Thus, antennas with similar proportions at different frequency ranges undergo the same changes in the characteristics of the antenna.

Looking at the single element of the antenna array, it can be said that the small ascertained pointing error is compensated by the symmetry of the antenna due to the central feed. Printed plastic is therefore suitable as material for the antenna array of the Ka-band PolInSAR system.

6.2 Improvements

In the following, a few aspects are listed which can be further improved, but were not carried out due to the time limit of this thesis.

- A temperature chamber that covers the actual expected temperature range would be an advantage, as it would allow investigation under real conditions. Especially the increase of tension between metalization and plastic of the printed antenna and, therefore, the detection of material fatigue would be possible.
- In order to qualify the strength of the metalization further, it would be advantageous to perform several temperature cycles.
- A suitable method must be found to preclude icing of the antenna. Possible approaches could be the controlled use of nitrogen or use of a climatic chamber which can regulate humidity as well as temperature.
- The artifacts occurring during transformation into time domain (horizontal brightened areas in Figure 5.5) could not be prevented and already be attributed to the Fourier transformation. The very reason of this effect should be examined in a further step to avoid errors during the transformation of the time gated signal back in frequency domain.

APPENDIX A

LISTING OF MEASUREMENT EQUIPMENT

Table A.1: List of non RF components.

Qty.	Component	Manufacturer	Designation	Description / Purpose
1x	Temperature chamber	Brabender	TSW 240/40 H	Tempering of the Antenna Under Test
1x	Polystyrene Plate	Austrotherm	XPS TOP 30 SF	Thermal-insulating coverage of climatic chamber.
1x	Multimeter	Fluke	287	Temperature measurement with temperature sensor.
1x	Temperature sensor	Fluke	80BK-A	Measurement of the AUT temperature.
1x	DC power supply	Hewlett Packard	E3631A	Power supply of the low noise amplifier.
1x	Linear axis	phytron	unknown	Accurate and reproducible positioning of the probe antenna.
1x	Motor controller	phytron	IXE α-C-T	Controlling the stepping motor of the linear axis.
1x	Laser	Bosch	GCL 25 Professional	Alignment of linear axis to climatic chamber.
1x	Probe antenna mounting	DLR	undefined	4 mm aluminum plate with 400 mm diameter and Ka-band waveguide mounting.
1x	AUT mounting	DLR	undefined	Mounting of the AUT in 0° to 90° elevation.
1x	Control Computer	undefined	undefined	PC with USB and RS232 interface to command the network analyzer and motor controller

Table A.2: List of RF components.

Qty.	Component	Manufacturer	Designation	Description / Purpose
1x	Network analyzer	Keysight Technologies	N9952A	Measurement of scattering parameters.
2x	RF cable	MegaPhase	RF Orange	2 m RF cable with 2.4 mm connectors to connect the network analyzer with AUT and LNA
2x	RF adapter	unknown	unknown	2.92 mm female to 2.4 mm male connector
2x	NMD port adapter	Tactron	CADP NMD2.4 F - 2.4F -50	NMD to 2.4 mm adapter to connect network analyzer ports with cables
2x	Waveguide to coax adapter	L3 Narda-ATM	28-25KPrA-6	2.92 mm female to WR28 waveguide transistion
1x	Adapter	API/Inmet	5171	2.92 mm male to 2.92 mm male adapter to connect transition at receiving side with LNA.
1x	Waveguide	L3 Narda-ATM	28-120A-7-6-7/AG	177.8 mm Ka-band waveguide to extend the probe antenne.
1x	Probe antenna	unknown	unknown	Probe antenna similar to an open ended waveguide.
1x	Horn antenna	L3 Narda-ATM	28-442-6	Test antenne to determine the influence of polystyrene.
1x	Low Noise Amplifier	B&Z Technologies	BZR-26004000-270833-202525	LNA for amplification of the measurement signal at the probe antenna.
1x	Pyramid RAM	E&C Anechoic Chambers NV	VHP-8	Absorber for covering the inside of the climatic chamber.
4x	Flat RAM	Cuming Microwave	C-RAM LF-73	
2x	Pyramid RAM	E&C Anechoic Chambers NV	VHP-4	Cover front side of the temperature chamber.
				Absorber collar of the probe antenna.

APPENDIX B

MATLAB CODE EXCERPTS

B.1 Network Analyzer Measurement

```
% perform measurement and return S2P struct
% FieldFox = VISA Object
function S2P = preformMeasurement(FieldFox)

    % set timeout to 40 s for long sweep times
    set(FieldFox,'Timeout',40)

    % Get number of traces
    fprintf(FieldFox,'CALCulate:PARameter:COUNt?');
    numberOfTraces = fscanf(FieldFox,'%i');

    % wait for all operations to completed
    fprintf(FieldFox,'INIT;*OPC?');
    trigComplete = fscanf(FieldFox,'%1d');

    % transfer stimulus data
    fprintf(FieldFox, 'FORM:DATA REAL,64\n');
    fprintf(FieldFox,'SENS:FREQ:DATA?\n');
    stimulus = binblockread(FieldFox,'double');
    hangLineFeed = fread(FieldFox,1);
    S2P = stimulus;

    % transfer trace data

    % set data format to real-32 bin block transfer
    fprintf(FieldFox,'FORM:DATA REAL,32');

    n = 0;
    while(n < numberOfTraces)

        % create string to read trace n
        TraceString = ['CALC:PAR',num2str(n+1),':SEL'];

        % select trace and set trace to linear
```

```
35          fprintf(FieldFox,TraceString);
36          fprintf(FieldFox,'CALC:FORMat MLINear');
37
38          % read data
39          fprintf(FieldFox,'CALC:DATA:SDATA?');
40          traceData = binblockread(FieldFox,'float');
41          hangLineFeed = fread(FieldFox,1);
42
43          % calculate S-Parameter and add to S2P matrix
44          S_re = traceData(1:2:end,:);
45          S_im = traceData(2:2:end,:);
46          S = S_re + (S_im * 1i);
47          S_mag = 20* log10(abs(S));
48          S_phase = angle(S) * 180 / pi;
49          S2P = [S2P, S_mag, S_phase];
50
51          % increment counter
52          n = n+1;
53      end
54
55      % reset timeout to 5 s
56      set(FieldFox,'Timeout',5)
57
58  end
```

B.2 Inverse Fourier Transform of a S2P Data Structure

```
% inverse fourier transformation of a S2P data structure
function ifftdata = ifftOfData(inputValues)

    % recalculate stimulus data
    startFreq = inputValues(1,1,1);
    stopFreq = inputValues(end,1,1);
    numOfFreq = size(inputValues,1);
    numOfAngles = size(inputValues,3);
    stimulus = transpose((0:1:(numOfFreq-1)) ./ (stopFreq-
    startFreq));
    stimulus = repmat(stimulus , [1,numOfAngles] );
    stimulus = reshape(stimulus,[numOfFreq,1,numOfAngles]);

    % ifft of S11
    S11_dB = inputValues(:,2,:);
    S11_lin = 10.^(S11_dB/20);
    S11_deg = inputValues(:,3,:);
    S11_rad = S11_deg .* (pi/180);
    S11_complex = S11_lin .* exp(1i * S11_rad);
    S11_fft_complex = (ifft(S11_complex));
    S11_fft_dB = 20*log10(abs(S11_fft_complex));
    S11_fft_deg = angle(S11_fft_complex) .* (180/pi);

    % ifft of S21
    S21_dB = inputValues(:,4,:);
    S21_lin = 10.^(S21_dB/20);
    S21_deg = inputValues(:,5,:);
    S21_rad = S21_deg .* (pi/180);
    S21_complex = S21_lin .* exp(1i * S21_rad);
    S21_fft_complex = (ifft(S21_complex));
    S21_fft_dB = 20*log10(abs(S21_fft_complex));
    S21_fft_deg = angle(S21_fft_complex) .* (180/pi);

    % ifft of S12
    S12_dB = inputValues(:,6,:);
    S12_lin = 10.^(S12_dB/20);
    S12_deg = inputValues(:,7,:);
    S12_rad = S12_deg .* (pi/180);
    S12_complex = S12_lin .* exp(1i * S12_rad);
    S12_fft_complex = (ifft(S12_complex));
    S12_fft_dB = 20*log10(abs(S12_fft_complex));
    S12_fft_deg = angle(S12_fft_complex) .* (180/pi);

    % ifft of S22
    S22_dB = inputValues(:,8,:);
```

```
45      S22_lin = 10.^(S22_dB/20);
46      S22_deg = inputValues(:,9,:);
47      S22_rad = S22_deg .* (pi/180);
48      S22_complex = S22_lin .* exp(1i * S22_rad);
49      S22_fft_complex = (ifft(S22_complex));
50      S22_fft_dB = 20*log10(abs(S22_fft_complex));
51      S22_fft_deg = angle(S21_fft_complex) .* (180/pi);
52
53      % combine in matrix
54      ifftdata = [stimulus S11_fft_dB S11_fft_deg S21_fft_dB
        S21_fft_deg S12_fft_dB S12_fft_deg S22_fft_dB S22_fft_deg];
55
56  end
```

B.3 Time Gating of Forward Transmission

```
% time gating of a signal in time domain
function gatedData = noiseSubstitutionGating(originalData,
    gateCenterMin, gateSpan, antennaDistance)

    % settings
    noiseHeight = 1;
    noiseOffset = -120;
    numOfPoints = 601;

    % constants
    c0 = 299792458; % m/s

    gatedData = originalData;
    angles = originalData.startAngle:originalData.stepSizeAngle
    :originalData.stopAngle;

    for angle = angles
        % calculate the upper and lower limit of the gate
        additionalLength = (antennaDistance / cosd(angle)) -
    antennaDistance;
        additionalTime = ((additionalLength/1000)/(c0)) * 10^9;
        gateCenter = gateCenterMin + additionalTime;
        gateBoarderMin = floor( (gateCenter - gateSpan) * 10);
        gateBoarderMax = ceil(  (gateCenter + gateSpan) * 10);

        % create arrays with noise
        randArray1 = (noiseHeight .* randn(gateBoarderMin,1)) -
     (noiseHeight/2) + noiseOffset;
        randArray2 = (noiseHeight .* randn(numOfPoints-
    gateBoarderMax+1,1)) - (noiseHeight/2) + noiseOffset;

        % calculate angle index
        angleIndex = int64(((angle - originalData.startAngle) /
     originalData.stepSizeAngle ) + 1);

        % apply gating data
        gatedData.timeValues(1:1:gateBoarderMin, 4, angleIndex)
     = randArray1;
        gatedData.timeValues(gateBoarderMax:1:numOfPoints, 4,
    angleIndex) = randArray2;
    end

end
```

ABBREVIATIONS

AUT	Antenna Under Test
CSV	Character Separated Values
CTE	Coefficient of Thermal Eexpansion
CTR	Compact Test Range
DLR	Deutsches Zentrum für Luft- und Raumfahrt (German Aerospace Center)
HFSS	High Frequency Structure Simulator (simulation software for electormagnetic structures from ANSYS, Inc.)
IF	Intermediate Frequency
LNA	Low Noise Amplifier
MATLAB	MATrix LABoratory (numerical computing software from MathWorks, Inc.)
RADAR	RAdio Detection And Ranging
RAM	Radiation Absorbent Material
RF	Radio Frequency
PolInSAR	Polarimetric Interferometric SAR
RS232	Recommended Standard 232 (serial computer interface)
S2P	Two port scattering paprameter file format
SAR	Synthetic Aperture Radar
SCPI	Standard Commands for Programmable Instruments
TE	Transverse Electric
USB	Universal Serial Bus
VF	Velocity Factor
VISA	Virtual Instrument Software Architecture

Frequency Band Designations

P-band	frequency range from 0.23 - 1.00 GHz
L-band	frequency range from 1.00 - 2.60 GHz
S-band	frequency range from 2.60 - 3.95 GHz
C-band	frequency range from 3.95 - 5.80 GHz
X-band	frequency range from 8.20 - 12.40 GHz
Ka-band	frequency range from 26.50 - 40.00 GHz

REFERENCES

[1] *Environmental Engineering Conditions and Laboratory Tests, MIL-STD-810G, 31-10-2008*, Department of Defense Test Method Standard, last accessed on 2018-11-27. [Online]. Available: http://everyspec.com/MIL-STD/MIL-STD-0800-0899/MIL-STD-810G_12306/

[2] J. C. Curlander and R. N. McDonough, *SYNTHETIC APERTURE RADAR: Systems and Signal Processing*. John Wiley & Sons, Inc., 1991, ISBN: 978-0-47-185770-9.

[3] *F-SAR: Airborne SAR Remote Sensing*, Deutsches Zentrum für Luft- und Raumfahrt e.V., Microwaves and Radar Institute, last accessed on 2019-02-22. [Online]. Available: https://www.dlr.de/Portaldata/32/Resources/dokumente/broschueren/F-SAR_Flyer_CD_druck.pdf

[4] A. Reigber, *DLR-Großinvestition: „Ka-Band PolInSAR Demonstrator“*, Deutsches Zentrum für Luft- und Raumfahrt e.V., Microwaves and Radar Institute, 03 2017, Rev: 1.0.

[5] Z. N. Chen, D. Liu, H. Nakano, X. Qing, and T. Zwick, *Handbook of Antenna Technologies*. Springer, Singapore, 2016, DOI: 10.1007/978-981-4560-44-3, ISBN: 978-981-4560-44-3.

[6] K. W. Kark, *Antennen und Strahlungsfelder: Elektromagnetische Wellen auf leitungen, im Freiraum und ihre Ausbreitung*, 6th ed. Springer Vieweg, Wiesbaden, 2017, ISBN: 978-3-658-13964-3.

[7] S. Silver, *Microwave Antenna Theory and Design*, 1st ed. McGraw-Hill Book Company, Inc., 1949.

[8] D. M. Pozar, *Microwave Engineering*, 4th ed. Addison-Wesley Publishing Company, Inc., 2012, ISBN: 978-0-47-063155-3.

[9] R. E. Collin, *Antennas and Radiowave Propagation*. McGraw-Hill Book Company, Inc., 1985, ISBN: 0-07-Y66156-1.

[10] J. L. Volakis, *Antenna Engineering Handbook*, 4th ed. McGraw-Hill Book Company, Inc., 2007, ISBN: 978-0-07-147574-7.

[11] W. Wang, J. Jin, J.-G. Lu, and S.-S. Zhong, "An untilted edge-slotted waveguide antenna array design." IEEE, 11 2004, DOI: 10.1109/ICCEA.2004.1459328, ISBN: 0-7803-8562-4 .

[12] C. A. Balanis, *Antenna Theory Analysis and Design*, 3rd ed. John Wiley & Sons, Inc., 2005, ISBN: 0-471-66782-X.

[13] D. Hoerni, *Polymer Materials pre-qualification for industrial applications*, SWISSto12 SA, 07 2017, Rev: 1.0.

[14] M. Basler and P. Tipler, *Physik: für Wissenschaftler und Ingenieure*, 7th ed., J. Wagner, Ed. Springer-Verlag Berlin Heidelberg, 2015, DOI 10.1007/978-3-642-54166-7, ISBN: 978-3-642-54166-7.

[15] *Werkstoffdatenblatt CuZn39Pb3*, Deutsches Kupferinstitut, last accessed on 2018-11-15. [Online]. Available: https://www.kupferinstitut.de/fileadmin/user_upload/kupferinstitut.de/de/Documents/Shop/Verlag/Downloads/Werkstoffe/Datenblaetter/Messing/CuZn39Pb3.pdf

[16] J. Reifenhäuser, *Investigation of Different Materials for Rectangular Waveguides in the Temperature Range from -55 to +30 °C*, 01 2019, Hochschule Koblenz, German Aerospace Center, Practical Report.

[17] W. Demtröder, *Experimentalphysik 1: Mechanik und Wärme*, 8th ed. Springer Spektrum, 2018, DOI 10.1007/978-3-662-46415-1, ISBN: 978-3-662-54847-9.

[18] *Produktdatenblatt: Stickstoff flüssig 5.0*, Linde AG, last accessed on 2019-02-15. [Online]. Available: https://produkte.linde-gase.de/db_neu/lin_5.0.pdf

[19] A. Newell and S. Gregson, "The effects of the absorber collar on open ended waveguide probes." AMTA 2009, Last accessed on 2019-02-15, 2009, NSI-MI Technologies. [Online]. Available: https://www.nsi-mi.com/images/Technical_Papers/2009/2009_AMTA_AN_The_Effect_of_the_Absorber-Collar_on_Open_Ended_Waveguide_Probes.pdf

[20] J. Eichler, *Physik für das Ingenieurstudium: Prägnant mit vielen Kontrollfragen und Beispielaufgaben*, 5th ed. Springer Vieweg, Wiesbaden, 2014, DOI 10.1007/978-3-658-04626-2, ISBN: 978-3-658-04626-2.

[21] *Time Domain Measurements using Vector Network Analyzer ZVR, Application Note 1EZ44_0E*, Rohde & Schwarz GmbH & Co. KG, last accessed on 2019-03-19. [Online]. Available: https://cdn.rohde-schwarz.com/pws/dl_downloads/dl_application/application_notes/1ez44/1ez44_0e.pdf

EIDESSTATTLICHE ERKLÄRUNG

Ich versichere, dass ich die vorliegende Arbeit selbständig verfasst und keine anderen als die angegebenen Quellen und Hilfsmittel benutzt habe. Die Arbeit wurde in gleicher oder ähnlicher Form noch keiner anderen Prüfungsbehörde vorgelegt und von dieser als Teil einer Prüfungsleistung angenommen. Alle Ausführungen, die wörtlich oder sinngemäß übernommen wurden, sind als solche gekennzeichnet.

_____

Oberpfaffenhofen, den 28. März 2019